NON-PEER-REVIEWED PREPRINT SUBMITTED TO EARTHARXIV. This manuscript has also been submitted to Next Sustainability (Elsevier) and is currently under peer review. This version (v1, 13 November 2026) has not been peer reviewed or accepted for publication, and its content may change. Please cite it as a preprint.

Uncertainty-aware deep learning for national lightning hazard and risk mapping to support sustainable disaster risk reduction in Bangladesh

Authors: Fardin Bin Faruque[1], Kazi Tahmid Parveg[2*], Jannatul Ferdous[3]

[1]Graduate Student, Department of Urban and Regional Planning, Khulna University of Engineering & Technology (KUET), Khulna-9203, Bangladesh. [fardintas40@gmail.com] (https://orcid.org/0009-0008-7521-6320)

[2]Graduate Student, Department of Urban and Regional Planning, Khulna University of Engineering & Technology (KUET), Khulna-9203, Bangladesh. [tahmidkazi2017012@gmail.com] (https://orcid.org/0009-0001-1044-5527)

[3]Graduate Student, Department of Urban and Regional Planning, Khulna University of Engineering & Technology (KUET), Khulna-9203, Bangladesh. [jannatulnova03@gmail.com] (https://orcid.org/0009-0006-4407-2163)

[*]Corresponding author

Corresponding author details

Corresponding author name: Kazi Tahmid Parveg

Mailing addresses: Department of Urban and Regional Planning, Khulna University of Engineering & Technology (KUET), Khulna-9203, Bangladesh

Email: tahmidkazi2017012@gmail.com

Highlights

• Deep-learning ensemble maps monthly lightning hazard across Bangladesh, 2012-2025

• All four networks beat climatology on unseen years; the ensemble cut error by 20 %

• An independent satellite climatology confirms the learned national hazard pattern

• A 2016 detection step in the ground record means no lightning trend is claimed

• 50 haor-basin upazilas (15.5 million people) are high risk with ≥ 90 % probability

Uncertainty-aware deep learning for national lightning hazard and risk mapping to support sustainable disaster risk reduction in Bangladesh

Abstract: Bangladesh has one of the world's highest lightning death tolls, borne mostly by farmers and fishers, yet national hazard maps rest on interpolation or tabular machine learning without independent validation. We developed a raster-native deep-learning framework reproducing monthly lightning stroke density from the WWLLN Global Lightning Climatology (WGLC, 2012-2025) on a 5-arc-minute grid from 18 meteorological, aerosol and surface predictors, comparing U-Net, Attention U-Net, ConvLSTM and a ConvLSTM-U-Net hybrid under a predefined protocol. On unseen years (2023-2025), every architecture outperformed monthly climatology, and a 12-member ensemble cut the mean squared error by 20 % and raised the hotspot critical success index from 0.15 to 0.27, whereas a convective available potential energy (CAPE) × precipitation proxy failed on hotspots (0.08). Recalibrated ensemble spread gave 90 % coverage of 95 % intervals. The ensemble matched the independent TRMM-LIS/ISS-LIS satellite climatology ($r = 0.53$) about as well as the ground record did, and Integrated Gradients ranked CAPE first in all 12 runs. A change-point test found a 2016 detection step (×1.96) in the observed record absent from the meteorological drivers, so no trend is claimed. With hazard, exposure and vulnerability combined under propagated uncertainty, risk peaks in the north-eastern haor basin, where 50 upazilas (15.5 million people) have probability ≥ 0.9 of being high or very high risk. District deaths follow pre-monsoon risk ($\rho = 0.40$) more closely than annual risk ($\rho = 0.19$), supporting harvest-timed warnings and shelters targeted to these upazilas under Sustainable Development Goal targets 1.5, 11.5 and 13.1.

Keywords: Lightning hazard; Disaster risk reduction; Deep learning; Uncertainty quantification; Explainable AI; Climate resilience; Bangladesh.

1. Introduction

Lightning kills people steadily, one or two at a time, mostly in rural areas and among people who work outdoors (Holle, 2016; Cooper and Holle, 2019). Bangladesh is an extreme case: its national database recorded 3,086 deaths between 1990 and mid-2016, with annual tolls rising sharply after 2010 (Dewan et al., 2017). After more than 60 people were killed on 12-14 May 2016, the Government declared lightning a natural disaster (Dewan et al., 2017; Ahmed et al., 2024). Most victims are farmers and fishers in open paddy fields and wetlands, and the deadliest weeks coincide with the *boro* rice harvest in April-May (Holle et al., 2019).

Over Bangladesh, warm and moist monsoon air meets dry continental air and steep orography. In the pre-monsoon season (March-May), conditional instability, dry-line boundaries and wind shear produce the severe local storms known as *Kalbaishakhi* or Nor'westers (Yamane et al., 2010a, 2010b). The haor wetland basin of Sylhet and Sunamganj, at the foot of the Meghalaya Plateau, is one of the regional hotspots in satellite climatology (Christian et al., 2003; Cecil et al., 2014; Albrecht et al., 2016; Dewan et al., 2018b). Lightning in Bangladesh is closely tied to convective available potential energy (CAPE) and convective rainfall (Dewan et al., 2018a). Recent work links transported dust and sulphate aerosol to the bimodal seasonal cycle, with peaks in April-May and around September (Azam et al., 2026), while pre-monsoon activity is also organised by thermodynamic and synoptic conditions (Rafiuddin et al., 2025). Aerosol-convection interactions are physically plausible (Rosenfeld et al., 2008; Yuan et al., 2011; Thornton et al., 2017) but hard to separate from meteorology in observations.

National hazard maps for Bangladesh nevertheless remain methodologically thin. Most studies interpolate fatality counts or thunderstorm days with inverse-distance weighting or kriging (Farukh et al., 2017; Ahmed et al., 2024), or relate district casualties to meteorological and socio-economic indicators with random forests, support vector machines or shallow neural networks (Mazumder and Saroar, 2025). Point-based tabular designs discard the spatial context that organizes convection, and random splits of autocorrelated samples inflate apparent skill (Roberts et al., 2017; Ploton et al., 2020). Hazard, exposure and vulnerability are also often mixed in a single target, so the resulting map cannot show which component drives the pattern.

Convolutional encoder-decoders such as U-Net learn multi-scale spatial structure directly from gridded fields (Ronneberger et al., 2015), attention gates weight the most relevant regions

(Schlemper et al., 2019), and convolutional long short-term memory (ConvLSTM) networks add temporal memory (Shi et al., 2015). These tools have transformed parts of Earth-system science (Reichstein et al., 2019), but in lightning research they have been used mainly for hourly nowcasting (Geng et al., 2019; Zhou et al., 2020; Leinonen et al., 2022), following earlier machine-learning work with meteorological predictors (Mostajabi et al., 2019). Monthly, national-scale hazard mapping raises three further questions. Does a deep network add anything beyond monthly climatology or a simple CAPE × precipitation proxy, in the tradition of simple convective lightning parameterizations (Price and Rind, 1992; Romps et al., 2014)? Can its output be trusted where it cannot be checked against training data? And does it learn physically sensible relationships or exploit artefacts (McGovern et al., 2019; Mamalakis et al., 2022)?

A fourth problem concerns the observations. Long ground-based records such as the World Wide Lightning Location Network (WWLLN) and the WGLC climatology derived from it (Virts et al., 2013; Kaplan and Lau, 2021) have a detection efficiency that varies in space and has grown over time (Rodger et al., 2006; Hutchins et al., 2012; Bürgesser, 2017). Models and trends built on them may therefore reflect network growth rather than climate, so validation against space-borne optical sensors (Blakeslee et al., 2020) and an explicit test for detection steps are needed. Finally, a hazard map is not a risk map. Disaster risk combines hazard, exposure and vulnerability (Crichton, 1999; Cardona et al., 2012; UNDRR, 2017), and a useful national product should carry hazard uncertainty through to the final ranking and be checked against observed casualties.

Reducing lightning deaths is also a sustainability problem. Most victims come from poor rural households whose livelihoods depend on outdoor work, so lowering lightning mortality speaks directly to the Sendai Framework target on disaster deaths and to Sustainable Development Goal (SDG) targets 1.5, 11.5 and 13.1 on the resilience of the poor, deaths from disasters and adaptive capacity to climate-related hazards (UNDRR, 2017). Meeting these targets with limited public resources requires knowing where shelters, lightning arresters and warnings would save the most lives, and how confident that judgement is.

This study addresses these gaps with a raster-native deep-learning framework for Bangladesh and asks four questions. RQ1: Do image-to-image networks reproduce monthly lightning stroke density better than climatological, persistence and physical-proxy baselines, and does architecture matter? RQ2: Do the learned patterns agree with an independent satellite climatology? RQ3:

Which predictors drive the predictions, and does the lightning record support trend claims? RQ4: Where is risk highest when hazard, exposure and vulnerability are combined with propagated uncertainty, and does the risk map relate to observed fatalities?

Accordingly, the objectives of this study are (i) to build a harmonized 5′ monthly data cube for Bangladesh (2012-2025) and benchmark four image-to-image deep-learning architectures against climatological, persistence and physical-proxy baselines; (ii) to validate the learned lightning hazard against an independent satellite climatology; (iii) to identify the predictors that drive the predictions and to test the lightning record for detection steps before any trend analysis; and (iv) to map upazila-level lightning risk from hazard, exposure and vulnerability with propagated uncertainty and to compare it with observed fatalities.

2. Methods and materials

2.1 Description of the study area

Bangladesh (20.6-26.6°N, 88.0-92.7°E; about 147,000 km² and 174 million people in 2025) occupies the lower Ganges-Brahmaputra-Meghna delta (Figure 1). Most of the country lies below 20 m, except the Chittagong Hill Tracts (CHT) in the south-east and the hills of the north-eastern border, where the Meghalaya Plateau rises to more than 1,500 m within a few tens of kilometers of Sylhet and Sunamganj. The north-eastern haor basin is a mosaic of seasonally flooded wetlands used for a single *boro* rice crop harvested in April-May. Four seasons are used throughout: pre-monsoon (March-May, MAM), monsoon (June-September, JJAS), post-monsoon (October-November, ON) and winter (December-February, DJF).

Models were trained on a buffered domain (86-94°E, 19-28°N) that gives the networks spatial context beyond the border, but all results are reported inside Bangladesh (1,773 grid cells) using the GADM 4.1 boundaries of the eight divisions, 64 districts and 545 level-3 units (GADM, 2022). The three CHT districts are treated as a ninth region because their terrain differs from the rest of Chittagong division.

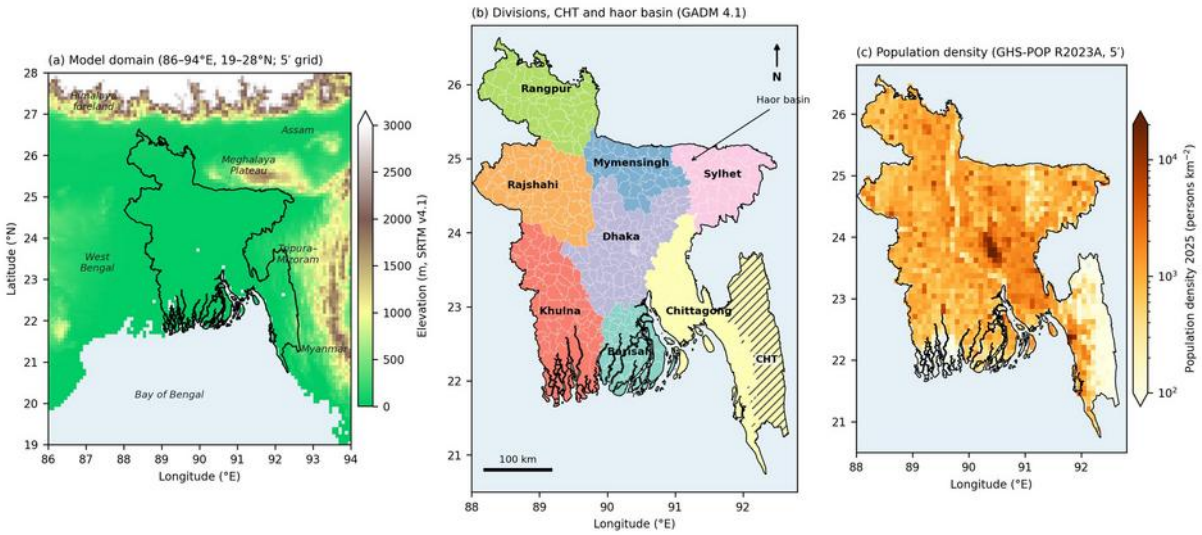


Figure 1. (a) Model domain on the 5′ grid (108 × 96 cells, 86-94°E, 19-28°N) with SRTM elevation, showing the buffer over neighboring India and Myanmar used for spatial context. (b) Administrative divisions of Bangladesh (GADM 4.1) with upazila boundaries, the Chittagong Hill Tracts (CHT, hatched) and the north-eastern haor basin. (c) 2025 population density aggregated to the 5′ grid (GHS-POP R2023A; national total 174.0 million).

2.2 Description of data

All data were harmonized to a 5-arc-minute (1/12°) grid of 108 × 96 cells aligned with the WGLC product, with monthly steps from January 2012 to December 2025 (Table 1). The years 2010-2011 were excluded because WWLLN was still expanding rapidly.

The target is the WWLLN Global Lightning Climatology and time series (WGLC; Kaplan and Lau, 2021), version v2026.0.0 (doi:10.5281/zenodo.20277101), which gives stroke density corrected for relative detection efficiency. WGLC counts cloud-to-ground and some strong intra-cloud strokes, not total lightning. Inside Bangladesh, the 2012-2021 mean of our data cube agreed with the published climatology at $r = 0.996$.

Dynamic predictors were ERA5 monthly single-level fields (Hersbach et al., 2020): CAPE, convective inhibition (CIN), the K and Total Totals (TT) indices, total column water vapor (TCWV), convective precipitation (CP), boundary-layer height (BLH), 2 m temperature and dew point (T2M, D2M) and 10 m wind components (U10, V10) with wind speed (WS). Rainfall came from CHIRPS v2.0 (Funk et al., 2015), day and night land-surface temperature from MODIS MOD11A2 (Wan et al., 2015), NDVI from MOD13A3 (Didan, 2015) and aerosol optical depth at

550 nm (AOD) from MERRA-2 (Gelaro et al., 2017; Randles et al., 2017), which was preferred because only about 46 % of monthly MODIS AOD retrievals were valid.

Static predictors were elevation, sub-grid elevation standard deviation (ELEV_SD) and slope from the SRTM v4.1 DEM (Jarvis et al., 2008), and crop, tree and water fractions, distance to water and a land mask from the Copernicus 100 m land cover for 2019 (Buchhorn et al., 2020). Fine layers were aggregated to 1 km in Google Earth Engine and block-averaged to the 5′ grid.

For independent validation, we used the combined TRMM-LIS (1998-2015) and ISS-LIS (2017-2023) annual flash-rate climatology at 0.1° (flashes km^{-2} yr^{-1}) from the LIS/OTD Reprocessed Flash Climatology distributed by the NASA Global Hydrometeorology Resource Center DAAC (cf. Cecil et al., 2014; Albrecht et al., 2016; Blakeslee et al., 2020). Optical sensors detect total lightning with nearly uniform detection efficiency but sparse sampling, about 218-265 h of view time per cell over Bangladesh. The product was used only for validation and sensitivity analysis.

The risk layers were never used as model inputs. Population for 2020 and 2025 came from GHS-POP R2023A (Schiavina et al., 2023), built-up fraction from GHS-BUILT-S R2023A (Pesaresi and Politis, 2023), night-time light (NTL) from the 2025 VIIRS annual composite (Elvidge et al., 2021) and travel time to the nearest city from the 2015 accessibility map (Weiss et al., 2018). District lightning deaths for 2015-2022 (64 districts; 2,142 deaths) were taken from Table 2 of Ahmed et al. (2024), which compiles Department of Disaster Management and NGO records. GHS-POP distributes census-based population estimates onto built-up areas, and its 2025 epoch is a model-based projection rather than a census count; the 2020 epoch was therefore retained as a sensitivity case (Section 2.15).

Table 1. Datasets, spatial and temporal resolution, and role in the framework.

Dataset	Variables	Native resolution	Period	Role	Reference
WGLC v2026.0.0 (WWLLN)	stroke density	5′, monthly	2012-2025	Target (Y)	Kaplan and Lau (2021)
ERA5 single levels	CAPE, CIN, KX, TT, TCWV, CP, BLH, T2M, D2M, U10, V10, WS	0.25°, monthly	2012-2025	Predictors	Hersbach et al. (2020)
CHIRPS v2.0	rainfall	0.05°, monthly	2012-2025	Predictor	Funk et al. (2015)
MODIS MOD11A2 / MOD13A3	LST day/night, NDVI	1 km, 8-day/monthly	2012-2025	Predictors	Wan et al. (2015); Didan (2015)
MERRA-2 M2TMNXAER	AOD 550 nm	0.5° × 0.625°	2012-2025	Predictor	Gelaro et al. (2017); Randles et al. (2017)
SRTM v4.1 (CGIAR)	elevation, ELEV_SD, slope	90 m	static	Predictors	Jarvis et al. (2008)
Copernicus GLS LC100	crop, tree, water fraction; distance to water; land mask	100 m	2019	Predictors/mask	Buchhorn et al. (2020)
TRMM-LIS / ISS-LIS	annual flash rate, viewtime	0.1°	1998-2015, 2017-2023	Independent validation	Cecil et al. (2014); Blakeslee et al. (2020)
GHS-POP R2023A	population count	30″ (≈1 km)	2020, 2025	Exposure	Schiavina et al. (2023)
GHS-BUILT-S R2023A	built-up fraction	100 m	2020	Exposure (sensitivity)	Pesaresi and Politis (2023)
VIIRS annual NTL	night-time radiance	15″	2025	Vulnerability	Elvidge et al. (2021)
MAP accessibility	travel time to cities	30″	2015	Vulnerability	Weiss et al. (2018)
GADM 4.1	country, division, district, upazila (level-3)	vector	-	Masks, aggregation	GADM (2022)

Dataset	Variables	Native resolution	Period	Role	Reference
District lightning deaths	deaths, injuries	district (n = 64)	2015-2022	Impact check	Ahmed et al. (2024)

Note: KX, TCWV, T2M, LST night, slope and elevation were removed by collinearity screening (Section 2.4); 18 predictors and a land-mask channel remained (Appendix Table A1).

2.3 Methodological framework

The workflow is summarized in Figure 2. Decision rules that could otherwise be tuned after seeing results (the model-selection score, the ensemble definition, the change-point rule and the risk formulation) were fixed before the relevant step was run, and the test years 2023-2025 played no role in any choice.

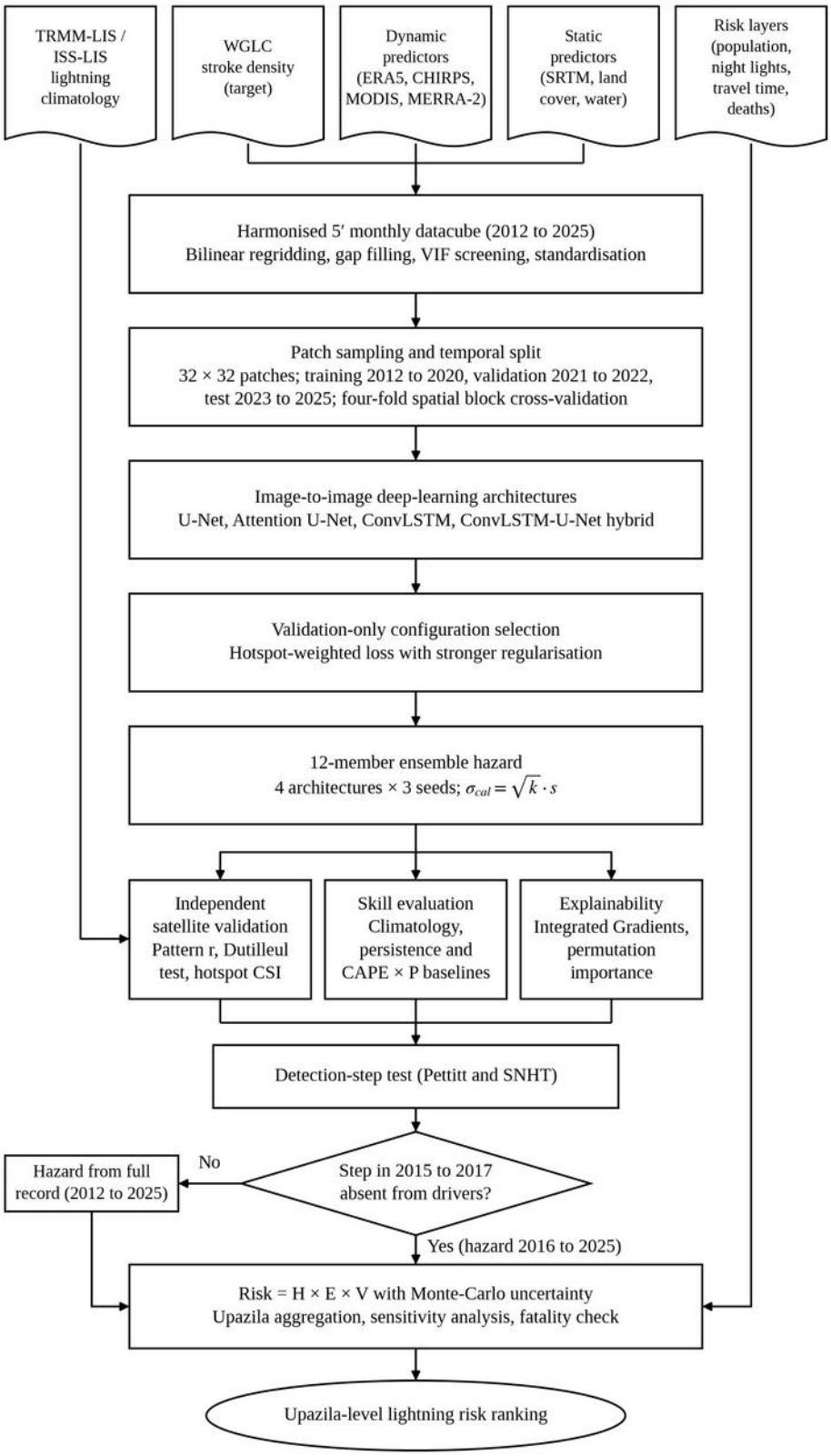


Figure 2. Methodological framework of the study.

2.4 Data cube construction and pre-processing

ERA5 and MERRA-2 fields were interpolated bilinearly to the 5′ grid (domain means changed by less than 1.7 %), CIN was set to zero where it is undefined, and MODIS gaps were filled after cloud screening (Appendix C).

The target was expressed in strokes km^{-2} yr^{-1} and log-transformed to stabilize its right-skewed distribution:

$$Y = \ln(1 + 365 \cdot \rho_{\mathrm{WGLC}}) \tag{1}$$

where ρ_{WGLC} is the monthly stroke density in strokes km^{-2} d^{-1}. Predictions are back-transformed with $\exp(Y) - 1$.

Collinearity among the 24 candidate predictors was screened on the training years (2012-2020) with the variance inflation factor,

$$\mathrm{VIF}_j = \frac{1}{1 - R_j^2} \tag{2}$$

where R_j^2 is the coefficient of determination from regressing predictor j on all others (O'Brien, 2007). Predictors with VIF > 10 were removed one at a time, with CAPE protected because of its physical role (Williams, 2005; Dewan et al., 2018a). T2M, the K-index, night-time LST, slope, TCWV and elevation were removed (maximum remaining VIF 8.3). U10 and V10 were retained because they encode flow direction, which separates the Nor'wester and monsoon regimes. The final input has 18 predictors and a land-mask channel (Appendix Table A1).

Skewed non-negative predictors were log-transformed ($g(x) = \ln(1 + x)$), and all channels were standardized with 2012-2020 statistics over the modelling mask:

$$\tilde{x}_c = \frac{g(x_c) - \mu_c}{\sigma_c} \tag{3}$$

Land-only channels were set to zero outside the modelling mask (7,741 cells, including 39 water-dominated cells inside Bangladesh), and the standardized mean drift in later years was below 0.14 σ.

2.5 Sampling and experimental design

Samples were 32 × 32-cell patches (about 290 km) with a stride of 8 cells at the 84 locations with at least 25 % land, each holding the predictors of months $t - 2$, $t - 1$ and t and the target of month t. The temporal split was fixed in advance: training 2012-2020, validation 2021-2022 and test 2023-2025 (8,904, 2,016 and 3,024 patch-months).

Spatial generalization was assessed with four-fold block cross-validation over north-west, north-east, south-west and south-east blocks (Appendix Figure B7a), removing every training patch that overlapped the held-out block (Roberts et al., 2017). The four fold models form a *CV mosaic* in which every cell is predicted by a model that never saw its block. Augmentation used random flips, with the sign of the matching wind component reversed.

2.6 Model architectures

Four image-to-image architectures were trained under identical conditions (Figure 3; Table 2), each mapping the input window to a 32 × 32 log-density field. U-Net (Ronneberger et al., 2015) has four encoder levels (32 to 256 channels) of double 3 × 3 convolutions with batch normalization and ReLU, and a transposed-convolution decoder with skip connections. Attention U-Net (Schlemper et al., 2019) adds additive attention gates to the skips, computing a weight map from the encoder features x_l and the gating signal g:

$$\alpha_l = \sigma\left(\psi^{\top}\mathrm{ReLU}\left(W_x x_l + W_g g + b_g\right) + b_\psi\right), \qquad \hat{x}_l = \alpha_l \odot x_l \tag{4}$$

Both U-Net variants read only the predictors of month t.

ConvLSTM (Shi et al., 2015) replaces the matrix products of an LSTM with convolutions, so hidden and cell states remain spatial maps. For input X_t and hidden state H_{t-1}, the gates are

$$\gamma_t = \sigma\left(W_{x\gamma} * X_t + W_{h\gamma} * H_{t-1} + b_\gamma\right), \qquad \gamma \in \{i,\ f,\ o\} \tag{5}$$

$$C_t = f_t \circ C_{t-1} + i_t \circ \tanh\left(W_{xc} * X_t + W_{hc} * H_{t-1} + b_c\right), \qquad H_t = o_t \circ \tanh\left(C_t\right) \tag{6}$$

where $*$ denotes convolution and $\circ$ the Hadamard product. We use two stacked ConvLSTM layers of 64 channels at full resolution, group-normalized gates and a 1 × 1 output head.

The ConvLSTM-U-Net hybrid applies a shared U-Net encoder to each month, runs a ConvLSTM with 112 channels on the 4 × 4 bottleneck, fuses the deepest features of the three months and decodes with skips from month t, so temporal memory enters at the most synoptic scale. All

networks include spatial dropout (p = 0.2), which allows Monte-Carlo dropout inference (Gal and Ghahramani, 2016).

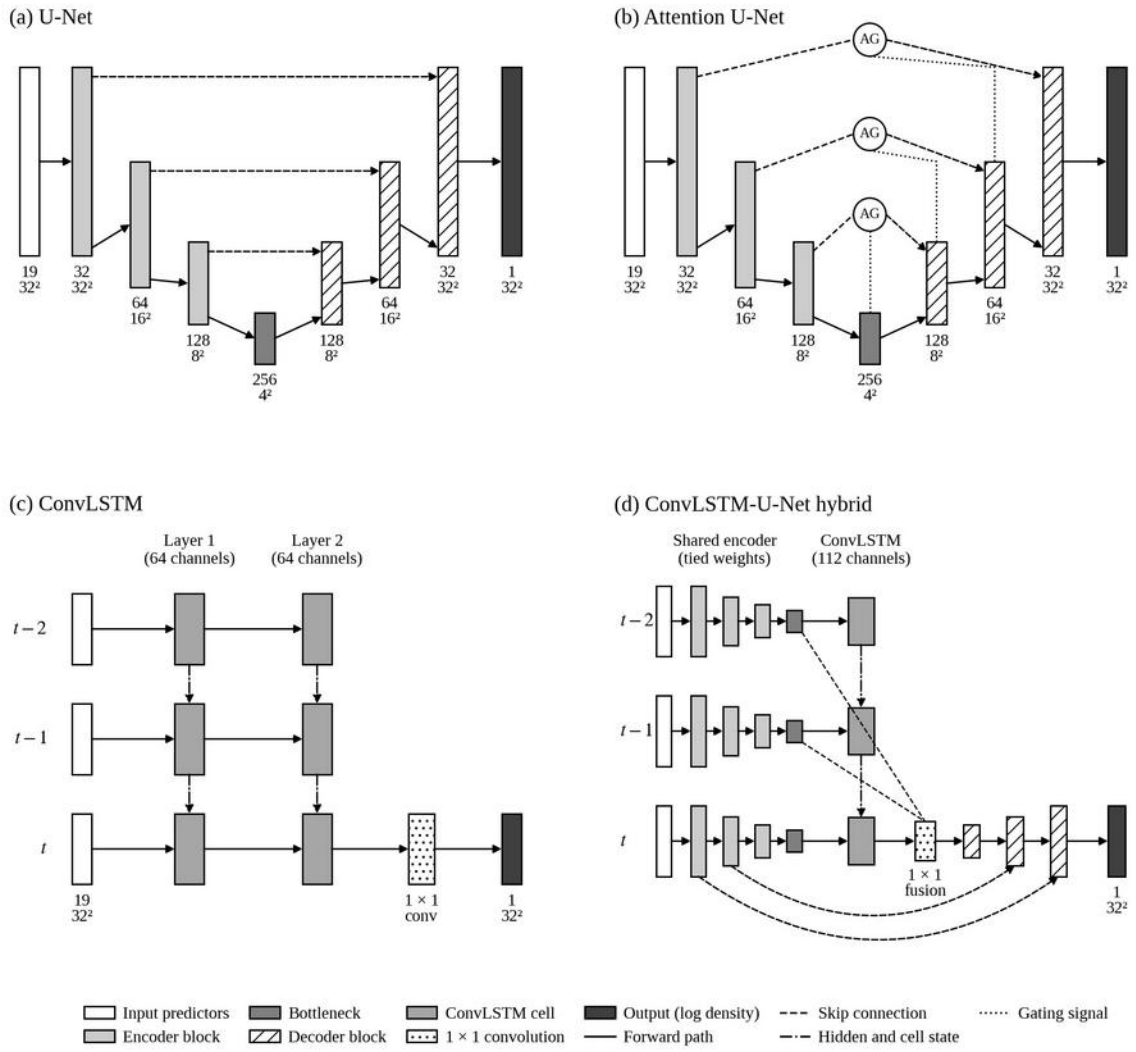


Figure 3. Architectures of the four image-to-image networks. (a) U-Net and (b) Attention U-Net map the 19-channel predictor stack of month t to log stroke density through four resolution levels; each block is a double 3 × 3 convolution with batch normalization and ReLU, down sampling uses max pooling and up sampling uses transposed convolution. In (b), the skip connections pass through additive attention gates (AG) driven by the coarser decoder signal. (c) ConvLSTM processes months t − 2, t − 1 and t at full 32 × 32 resolution with two stacked layers, and a 1 × 1 convolution maps the final hidden state to the output. (d) The ConvLSTM-U-Net hybrid applies a shared encoder to the three months, runs a ConvLSTM on the 4 × 4 bottleneck, fuses the deepest features of the three months and decodes with skips from month t. Numbers below blocks give feature channels and spatial size; parameter counts are listed in Table 2.

Table 2. Architectures and training configuration (final variant v5).

Model	Parameters	Input months	Key components
U-Net	1,931,617	t	4 levels (32-256 ch), DoubleConv + BN + ReLU, transposed-conv upsampling, 3 skips
Attention U-Net	1,953,687	t	U-Net + additive attention gates on all 3 skips (Eq. 4)
ConvLSTM	487,745	t − 2, t − 1, t	2 × ConvLSTM (64 hidden, 3 × 3), GroupNorm on gates, inter-layer dropout, 1 × 1 head
ConvLSTM-U-Net hybrid	1,990,561	t − 2, t − 1, t	shared encoder, ConvLSTM (112 hidden) on 4 × 4 bottleneck, fused deepest skip
Common settings	-	-	AdamW (lr 3×10^{-4}, weight decay 10^{-3}); batch 32; ReduceLROnPlateau (×0.5, patience 4); early stopping (patience 12, max 80 epochs); gradient clipping 5; fp16 mixed precision; Dropout2d p = 0.2; seeds 42, 43, 44

2.7 Training objective and configuration selection

Models were trained with AdamW (Loshchilov and Hutter, 2019) in fp16 mixed precision (Micikevicius et al., 2018) using PyTorch (Paszke et al., 2019), with learning-rate halving and early stopping on validation RMSE. The loss combines a masked, hotspot-weighted squared error with a structural-similarity term (Wang et al., 2004):

$$\mathscr{L} = \frac{\sum_i m_i w_i \left(\hat{y}_i - y_i\right)^2}{\sum_i m_i w_i} + \lambda \left(1 - \mathrm{SSIM}(\hat{y},\, y)\right), \qquad w_i = 1 + \alpha y_i \tag{7}$$

where m_i is the modelling mask, y_i the log-density target, $\lambda = 0.1$ and α sets the hotspot weight ($\alpha = 0$ gives the plain masked error).

An initial baseline (v1: $\alpha = 0$) produced over-smooth maps that underestimated the Sylhet hotspot by about half. Three modifications were therefore tested: a leakage-free climatological prior channel, the hotspot-weighted loss ($\alpha = 1$) and stronger regularization. Five variants were trained with all four architectures and scored on the 2021-2022 validation years with a criterion fixed beforehand: the mean of log RMSE, physical RMSE and 1 − CSI for the top-20 % hotspot cells,

each relative to v1. The selected variant (v5: hotspot loss and regularization, without the prior; Table 3) was then trained with three seeds per architecture.

Table 3. Validation-only ablation (2021-2022, inside Bangladesh, mean of the four architectures, seed 42). Lower selection score is better; the predefined rule selected v5.

Variant	Prior	Hotspot loss	Regul.	Score	RMSE (log)	R^2	RMSE (phys)	CSI	POD	FAR	Hot ratio
v1_base	-	-	-	1.000	0.520	0.484	2.65	0.261	0.296	0.303	0.31
v2_clim	√	-	-	0.985	0.521	0.482	2.63	0.290	0.344	0.350	0.33
v3_clim_hot	√	√	-	0.956	0.522	0.481	2.60	0.348	0.452	0.396	0.37
v4_clim_hot_reg	√	√	√	0.953	0.518	0.488	2.58	0.345	0.446	0.392	0.38
v5_hot_reg (selected)	-	√	√	0.948	0.528	0.468	2.54	0.359	0.496	0.431	0.41
Climatology				-	0.585	0.348	-	0.215	-	-	0.29

Hot ratio = mean predicted ÷ mean observed intensity inside observed top-20 % cells (physical units). RMSE (phys) in strokes km^{-2} yr^{-1}.

2.8 Ensemble, full-domain inference and baselines

Full-domain maps were obtained by averaging overlapping patch predictions. The hazard layer is a 12-member ensemble (four architectures × three seeds) averaged in log space:

$$\hat{y}_{\text{ens}} = \frac{1}{12} \sum_{a=1}^{4} \sum_{s=1}^{3} \hat{y}_{a,s} \tag{8}$$

Three non-learning baselines were used: (i) climatology, the 2012-2020 mean of each calendar month; (ii) persistence, the value 12 months earlier; and (iii) a physical proxy, ln(1 + CAPE × P) with P the CHIRPS rainfall, mapped to the target by isotonic regression (Barlow et al., 1972) fitted on training months. CAPE × precipitation is a widely used convective lightning parameterization (Romps et al., 2014).

2.9 Evaluation metrics and significance testing

Skill was computed inside Bangladesh on the test period, overall and by season:

$$\text{RMSE} = \sqrt{\frac{1}{N} \sum_{i=1}^{N} (\hat{y}_i - y_i)^2}, \qquad \text{MSESS} = 1 - \frac{\text{MSE}_{\text{model}}}{\text{MSE}_{\text{clim}}} \tag{9}$$

We also report MAE, bias, Pearson r, R^2, SSIM and the pattern correlation of the period-mean map. Hotspots are cells at or above the observed 80th percentile, with the same threshold applied to predictions. With hits H, misses M and false alarms F,

$$\text{POD} = \frac{H}{H+M}, \qquad \text{FAR} = \frac{F}{H+F}, \qquad \text{CSI} = \frac{H}{H+M+F} \tag{10}$$

A random forecast scores CSI ≈ 0.11. The hotspot intensity ratio compares mean predicted and observed intensity inside observed hotspots, and hotspot scores are undefined in most of DJF.

Systems were compared on the 36 monthly Bangladesh-mean RMSEs and monthly CSIs with paired Wilcoxon signed-rank tests (Wilcoxon, 1945) and Holm correction (Holm, 1979). Because monthly errors are serially correlated, 95 % confidence intervals of mean differences came from a moving-block bootstrap (block length 3 months, 5,000 resamples; Künsch, 1989).

2.10 Predictive uncertainty

Three uncertainty estimates were compared: Monte-Carlo dropout (30 passes per run; Gal and Ghahramani, 2016), the spread across seeds, and the spread s across all 12 members

(Lakshminarayanan et al., 2017). In a well-calibrated ensemble the spread matches the error of the ensemble mean (Fortin et al., 2014), but small deep ensembles are often under-dispersive, so the spread was rescaled with a factor fitted on the validation years:

$$k = \left.\frac{\sum e^2}{\sum s^2}\right|_{2021–2022}, \qquad \sigma_{\text{cal}} = \sqrt{k} \cdot s \tag{11}$$

where e is the ensemble-mean error. Calibration was assessed by the coverage of 68 % and 95 % intervals, the spread-skill ratio, the continuous ranked probability score (CRPS; Gneiting and Raftery, 2007) and probability-integral-transform (PIT) histograms.

2.11 Independent validation against the satellite climatology

Because WGLC counts strokes and LIS counts total flashes, with different detection efficiencies and periods, agreement was assessed on spatial patterns, with each map divided by its Bangladesh mean. The primary comparison used exact area-weighted means on 46 blocks of 0.5° with at least half their area in Bangladesh, and a secondary comparison used the 5′ grid.

Correlations were tested with the modified *t*-test of Dutilleul (1993), using effective sample sizes from Moran's *I* correlograms (Moran, 1950; Clifford et al., 1989), with confidence intervals from a spatial block bootstrap (1° tiles). A Poisson noise ceiling from the raw flash counts bounds the attainable correlation. Hotspot and regional-rank agreement were also compared.

2.12 Explainability

Integrated Gradients (IG; Sundararajan et al., 2017), implemented in Captum (Miglani et al., 2023), attributes a scalar output F to each input by integrating gradients from a baseline x' to the input x:

$$\mathrm{IG}_c(x) = \left(x_c - x_c'\right) \int_0^1 \frac{\partial F\left(x' + \alpha(x - x')\right)}{\partial x_c} \, d\alpha \tag{12}$$

Targets were the mean predicted log-density over Bangladesh, Sylhet division and the CHT for each test month and all 12 runs, with the all-zero standardized input (the 2012-2020 mean state) as baseline. Channel importance is the share of mean absolute attribution, and agreement between runs was measured with Kendall's W (Kendall and Babington Smith, 1939). Permutation importance (Breiman, 2001) of single channels and six physical groups provided a model-agnostic cross-check (Appendix C).

Permutation importance (Breiman, 2001) provided a model-agnostic cross-check. It is the increase in test RMSE, and the loss of hotspot CSI, when a predictor is permuted (five repeats). Dynamic predictors were permuted by shuffling whole monthly maps across the 38 months feeding the test windows. Static predictors were permuted by shuffling 1° tiles among land tiles. Correlated predictors were also permuted jointly within six physical groups: precipitation, thermodynamic, wind, aerosol, surface, and terrain/land cover. Attention-gate maps of the Attention U-Net were inspected but are reported only in the Appendix because they were unstable across seeds.

2.13 Detection-step test and trend analysis

Before any trend analysis, annual and depersonalized monthly Bangladesh-mean series of the observations, the ensemble, CAPE, CHIRPS, CAPE × P and the residuals were tested for abrupt steps with the Pettitt test (Pettitt, 1979) and the standard normal homogeneity test (SNHT; Alexandersson, 1986). The Pettitt statistic is

$$U_t = \sum_{i=1}^{t} \sum_{j=t+1}^{n} \operatorname{sgn}\left(x_i - x_j\right), \qquad K = \max_t |U_t| \tag{13}$$

The record was to be classified as *detection-affected* if the observed series showed a significant step ($p < 0.05$) beginning in 2015-2017 that none of CAPE, CHIRPS or CAPE × P shared within ±1 year, in which case trends would be estimated only after the step. Pixel-wise trends used the Mann-Kendall test (Mann, 1945; Kendall, 1975) and the Sen slope (Sen, 1968):

$$S = \sum_{i<j} \operatorname{sgn}\left(x_j - x_i\right), \qquad \beta = \operatorname{median}\left(\frac{x_j - x_i}{j - i}\right) \tag{14}$$

Multiplicity was controlled with the Benjamini-Hochberg false discovery rate at $q = 0.05$ (Benjamini and Hochberg, 1995), and field significance was assessed by permuting years (Livezey and Chen, 1983; Wilks, 2016).

2.14 Risk mapping

Risk was defined on the 5′ grid as the product of normalized hazard, exposure and vulnerability (Crichton, 1999; Cardona et al., 2012). The hazard H is the mean ensemble stroke density over 2016-2025, the period after the detection step (Section 3.6); the modelled hazard was preferred for the reasons discussed in Section 4, with the observed WGLC hazard kept as a sensitivity case. Exposure E is log population density in 2025, and vulnerability V combines inverse night-time

light (poverty and poor electrification) with travel time (remoteness from care). Each component was scaled onto [0.05, 1] between the 2nd and 98th percentiles:

$$n(x) = 0.05 + 0.95 \cdot \min\left[1,\ \max\left(0,\ \frac{x - P_2}{P_{98} - P_2}\right)\right] \tag{15}$$

$$V = n\left(\sqrt{(1 - n(\ln(1 + \mathrm{NTL}))) \cdot n(\ln(1 + T))}\right), \qquad R = n(H) \cdot n\left(\ln\left(1 + D_{\mathrm{pop}}\right)\right) \cdot V \tag{16}$$

where T is travel time and D_{pop} population density. Risk was classified into quintiles and aggregated to the 545 upazilas as area-weighted means, which form the primary product because the hazard is more reliable at regional than at cell scale (Section 3.3). Fisher-Jenks natural breaks (Jenks, 1967) served as a classification sensitivity test. Upazila populations were obtained with the same fractional overlay of 10 × 10 sub-cells per grid cell, which captures 99.6 % of the national population. The 545 units are GADM level-3 units, which list urban thanas and city corporation areas separately and therefore outnumber the roughly 495 official upazilas.

2.15 Risk uncertainty and sensitivity

The calibrated monthly predictive standard deviation was propagated to the ten-year mean hazard by the delta method, assuming an exchangeable correlation ρ between monthly errors:

$$\sigma_{\bar{h}}^2 = \frac{1}{N^2}\left[\sum_t \sigma_t^2 + \rho \sum_{t \neq t'} \sigma_t \sigma_{t'}\right], \qquad H^{(b)} = \bar{H} \cdot \exp\left(\sigma_{\log H}\, z^{(b)}\right) \tag{17}$$

ρ was set by coverage calibration on the 2021-2022 mean map (ρ = 0.07; Appendix C), and 1,000 log-normal hazard realizations were drawn, spatially coherent for upazila statistics. An upazila's class was flagged *uncertain* if its modal-class probability was below 0.6, and P(high or very high) is reported as a decision layer.

Ranking sensitivity was assessed under alternative weights, hazard periods, scaling and sources (observed WGLC and the satellite climatology), exposure definitions and vulnerability definitions, using Spearman correlation, top-50 overlap and the share of upazilas changing class. Seasonal risk (MAM, JJAS and September) used seasonal hazard means.

2.16 Fatality check

District mean risk and hazard were compared with 2015-2022 lightning deaths (Ahmed et al., 2024), expressed per area and per capita, using Spearman correlation. The primary annual risk was

fixed before the fatality data were examined, and 26 layers were compared in total. Because the fatality table covers about 73 % of the national totals of the Department of Disaster Management (Mongabay, 2026) and spatial autocorrelation was not modelled, the comparison is exploratory.

3. Results

3.1 Lightning climatology of Bangladesh, 2012-2025

The WGLC record shows a bimodal seasonal cycle (Figure 4). Bangladesh-mean stroke density rises to a broad pre-monsoon and early-monsoon plateau (2.32, 2.68 and 2.91 strokes km^{-2} yr^{-1} in April, May and June), falls to a July minimum (1.13) and peaks again in September (3.28). CAPE follows a similar two-peaked cycle. The monsoon accounts for 52.9 % of annual strokes, MAM for 35.5 % and ON for 10.1 %, in agreement with Azam et al. (2026).

In the pre-monsoon, activity concentrates along the Meghalaya foothills in Sunamganj and Sylhet (April regional mean 5.6 strokes km^{-2} yr^{-1}), where all ten most active cells lie. In September, the CHT become as active as the north-east (regional mean 5.40), and the north-west is also relatively active (Figure 4d-f). Activity in 2012-2015 was markedly lower than in later years (Figure 4a; Section 3.6).

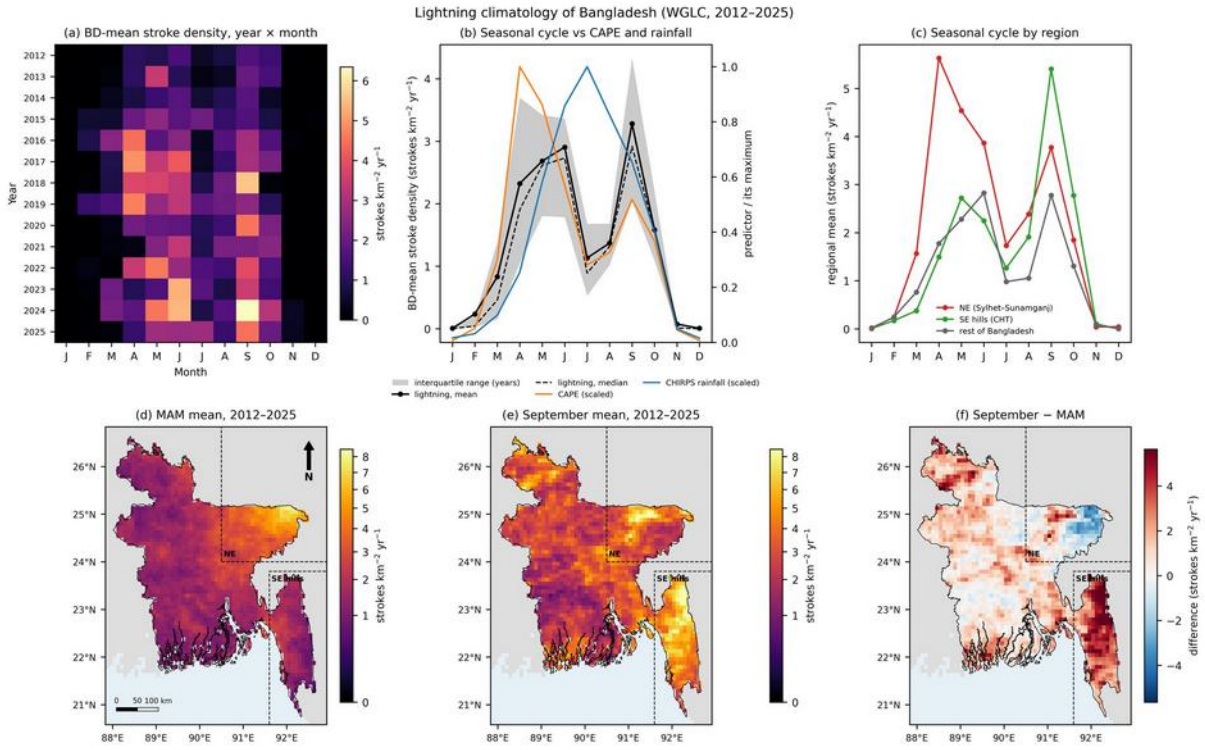


Figure 4. Lightning climatology of Bangladesh from WGLC, 2012-2025. (a) Bangladesh-mean stroke density by year and month; (b) mean seasonal cycle with CAPE and CHIRPS rainfall scaled to their maxima; (c) seasonal cycles of the north-east, the CHT and the rest of the country; (d) MAM mean, (e) September mean and (f) September minus MAM.

3.2 Skill on unseen years and the value of deep learning

The validation-only ablation (Table 3; Appendix Figure B8) identified the hotspot-weighted loss as the most useful change, raising the validation hotspot CSI from 0.26 to 0.35 at almost unchanged RMSE. The climatological prior added nothing once the other changes were in place, which shows that the networks did not rely on a location-specific memory of past lightning.

On the 2023-2025 test years, all architectures and the ensemble outperformed climatology and persistence on every bulk metric (Table 4; Figure 5). The ensemble reduced the log RMSE from 0.666 to 0.596 (MSESS 0.20), explained 41 % of the cell-month variance (R^2 = 0.414 against 0.269) and nearly doubled the pooled hotspot CSI (0.27 against 0.15). Persistence was the worst bulk predictor (MSESS = −0.55) but had the highest pattern correlation (0.88), because it copies the previous year's structure. Architectures differed little (test RMSE from 0.606 for ConvLSTM to 0.621 for U-Net), and the ConvLSTM matched the best skill with about a quarter of the parameters.

Table 4. Test-period skill (2023-2025, all months, inside Bangladesh; log1p space unless stated). Architectures: mean ± SD over three seeds.

System	RMSE	R^2	RMSE phys	SSIM	CSI	POD	FAR	Hot ratio	MSESS	Pattern r
U-Net	0.621 ± 0.006	0.365 ± 0.013	3.36	0.355	0.272	0.357	0.462	0.33	0.131	0.67
Attention U-Net	0.608 ± 0.006	0.392 ± 0.012	3.34	0.360	0.299	0.389	0.437	0.33	0.168	0.70
ConvLSTM	0.606 ± 0.005	0.395 ± 0.010	3.34	0.336	0.284	0.372	0.444	0.34	0.172	0.68
ConvLSTM-U-Net	0.615 ± 0.013	0.377 ± 0.026	3.35	0.350	0.272	0.354	0.456	0.32	0.147	0.71
Ensemble (12)	0.596	0.414	3.33	0.346	0.274	0.337	0.407	0.32	0.199	0.70
Climatology	0.666	0.269	3.56	0.292	0.150	0.174	0.479	0.22	0.000	0.68
Persistence (t − 12)	0.828	−0.130	4.53	0.284	0.272	0.433	0.577	0.54	−0.545	0.88
CAPE × P (linear)	0.684	0.230	3.73	0.240	0.000	0.000	-	0.13	−0.053	0.50
CAPE × P (monotonic)	0.621	0.364	3.52	0.302	0.076	0.078	0.249	0.22	0.130	0.43

RMSE phys in strokes km^{-2} yr^{-1}. Pattern r of architectures refers to seed-mean maps. Hotspot = top 20 % of observed cell-months (threshold applied to predictions).

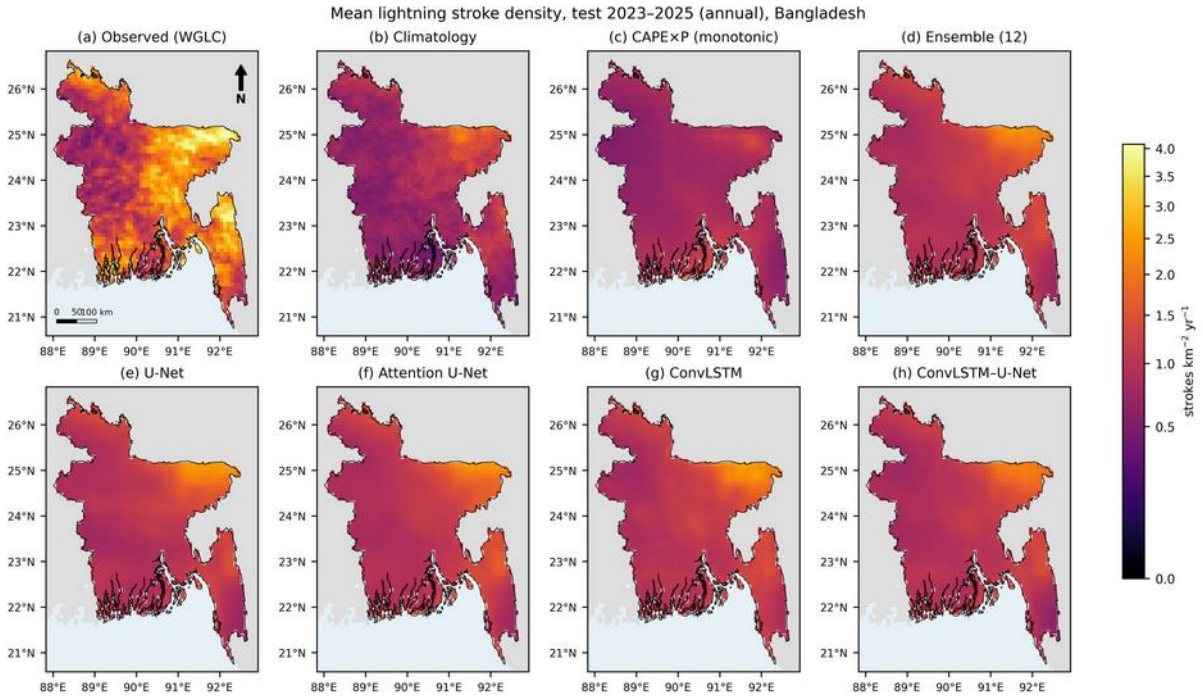


Figure 5. Mean stroke density for the test years 2023-2025: (a) observed WGLC, (b) monthly climatology, (c) CAPE × P proxy, (d) 12-member ensemble and (e-h) seed-mean maps of the four architectures. Pre-monsoon and bias maps are given in Appendix Figures B1 and B3.

Paired tests confirmed these gains (Figure 6; Appendix Table A5). Every architecture beat climatology on monthly RMSE after Holm correction (p = 0.009-0.029), and the ensemble did so with p = 0.002 (mean difference −0.060; 95 % CI −0.098 to −0.029; better in 78 % of months). Only one of six architecture pairs differed (Attention U-Net better than U-Net by 0.011, p = 0.029). Against the monotonic CAPE × P proxy, no model differed on monthly RMSE (ensemble p = 1.0), so two physical variables capture most of the bulk variance.

Spatial structure told a different story. The proxy placed hotspots poorly (pooled CSI 0.08, pattern r 0.43), and all architectures beat it on monthly CSI (p = 0.002-0.022). Month by month, however, no model placed hotspots better than climatology, and persistence had the highest monthly CSI (0.154 against 0.075 for the ensemble). The pooled CSI advantage therefore comes mainly from predicting which months and seasons are active.

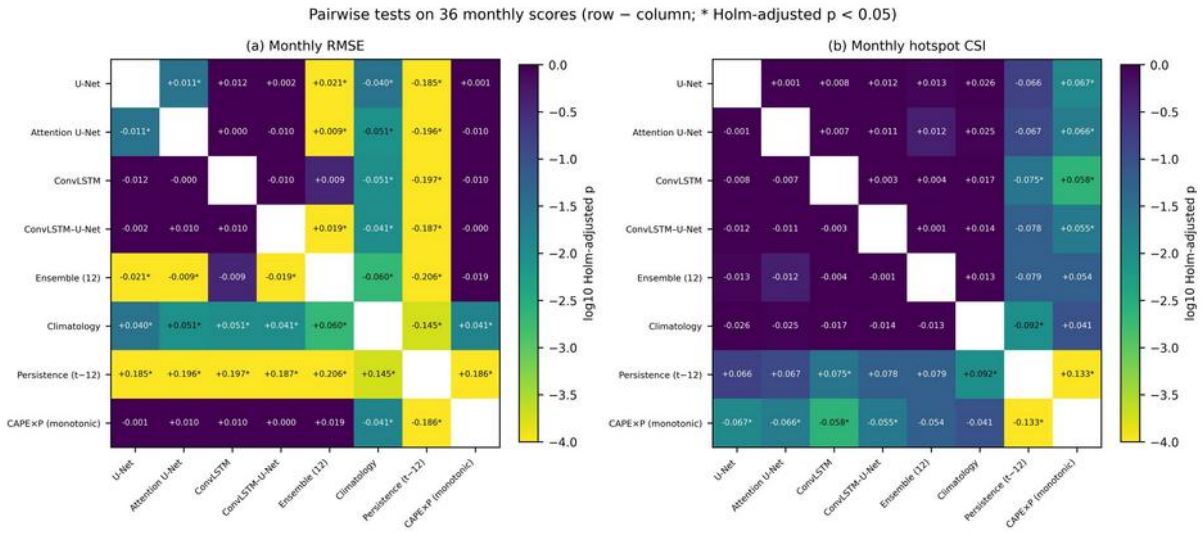


Figure 6. Pairwise tests on the 36 monthly test scores (row minus column). (a) Monthly RMSE; (b) monthly hotspot CSI (24 months with a defined hotspot set). Colors show $\log_{10}$ of the Holm-adjusted Wilcoxon *p*-value; asterisks mark $p < 0.05$. Negative RMSE differences and positive CSI differences favor the row system.

Gains over climatology were largest in the pre-monsoon (MSESS 0.29; R^2 0.30 against 0.02) and post-monsoon (MSESS 0.25), when year-to-year differences in storm activity are large, and modest in the monsoon (MSESS 0.12; Table 5; Appendix Figure B2). All models compressed spatial contrasts (hotspot intensity ratio 0.32 for the ensemble), and the most prominent failure was the south-eastern hills in September, where observed densities of about 5 strokes km^{-2} yr^{-1} were predicted as 1.0-1.3.

Table 5. Seasonal test-period skill of the ensemble and the baselines (inside Bangladesh, log1p space).

Season	System	RMSE	R^2	Bias	CSI	MSESS	Pattern r
MAM	Ensemble (12)	0.640	0.303	+0.159	0.252	0.290	0.75
	Climatology	0.759	0.019	+0.055	0.164	0	0.66
	CAPE × P (monotonic)	0.680	0.213	−0.125	0.092	0.198	0.54
	Persistence	1.009	−0.733	+0.099	0.192	−0.766	0.88
JJAS	Ensemble (12)	0.765	0.192	−0.030	0.071	0.124	0.57
	Climatology	0.818	0.077	−0.242	0.022	0	0.54
	CAPE × P (monotonic)	0.791	0.136	−0.100	0.008	0.064	0.30
	Persistence	0.976	−0.314	−0.034	0.239	−0.424	0.84

Season	System	RMSE	R^2	Bias	CSI	MSESS	Pattern r
ON	Ensemble (12)	0.570	0.303	−0.084	0.124	0.250	0.12
	Climatology	0.659	0.071	−0.204	0.027	0	−0.05
	CAPE × P (monotonic)	0.597	0.236	−0.139	0.001	0.178	0.16
	Persistence	0.803	−0.383	−0.053	0.197	−0.488	0.79
DJF	Ensemble (12)	0.128	-	+0.019	n/a	0.151	0.05
	Climatology	0.139	-	+0.044	n/a	0	0.02

DJF: ≥ 80 % of cell-months have no strokes, so hotspot scores are undefined (n/a) and R^2 is not meaningful.

3.3 Predictive uncertainty and spatial generalization

Raw Monte-Carlo dropout was badly over-confident, with 95 % intervals covering only 5.6 % of observations (Table 6; Figure 7). The raw ensemble spread was more realistic but still under-dispersive (95 % coverage 0.53). Rescaling the variance by $k = 12.7$ gave 95 % and 68 % coverage of 0.90 and 0.70 on the test years, a spread-skill ratio of 0.88 and the lowest CRPS (0.291).

Table 6. Uncertainty calibration on the test years (inside Bangladesh, log1p space).

Method	Mean σ	68 % coverage	95 % coverage	Spread-skill	CRPS
MC dropout (raw, mean of runs)	0.026	0.018	0.056	0.04	0.398
Seed spread, single architecture (raw)	0.11-0.16	0.12-0.26	0.34-0.46	0.18-0.27	0.346-0.366
Ensemble spread (raw)	0.146	0.263	0.534	0.25	0.345
Ensemble spread × √k (primary)	0.522	0.698	0.903	0.88	0.291
Ensemble, affine $\sigma^2 = a + b\, s^2$	0.629	0.759	0.937	1.05	0.291

k = 12.71 and (a, b) = (0.0008, 18.40) fitted on 2021-2022. Nominal coverage: 0.68 and 0.95; ideal spread-skill ratio: 1.

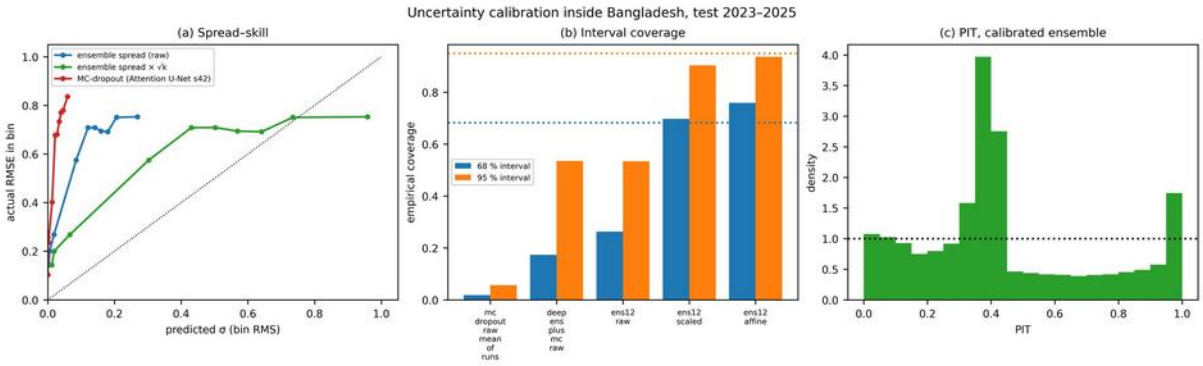


Figure 7. Uncertainty calibration inside Bangladesh, test 2023-2025. (a) Spread-skill: binned predicted σ against actual RMSE for raw ensemble spread, calibrated spread (× √k) and MC dropout; the dotted line is perfect calibration. (b) Empirical coverage of nominal 68 % and 95 % intervals (dotted lines). (c) PIT histogram of the calibrated ensemble.

Spatial generalization was weaker than temporal generalization (Appendix Table A3; Figure B7). The CV ensemble reached RMSE 0.636, R^2 0.334 and CSI 0.26, still better than climatology on RMSE and CSI even though climatology uses the local history of the held-out block. In the north-west block no model beat climatology, whereas the hybrid transferred best to the north-eastern hotspot (R^2 0.43 against 0.29 for climatology).

3.4 Independent validation against the satellite climatology

Against the satellite climatology, the WGLC target agreed at r = 0.63 (95 % CI 0.37-0.82; Dutilleul p = 0.028; effective $n \approx 12$; Table 7; Figure 8). The ensemble on the unseen test years agreed at r = 0.53 (CI 0.35-0.71), slightly higher than the WGLC observations of the same years (r = 0.46), although its Dutilleul test was marginal (p = 0.066). The agreement is therefore positive and no lower than that of the observations. The CAPE × P proxy showed no agreement (r = 0.05) and a chance-level hotspot CSI (0.11).

Table 7. Pattern agreement with the independent TRMM-LIS/ISS-LIS climatology (primary comparison: 46 exact 0.5° blocks, each map divided by its Bangladesh mean).

Product	r [95 % CI]	n_{eff}	p (Dutilleul)	ρ	CSI top 20 %	Δr vs WGLC same period [95 % CI]
WGLC observed 2012-2025 (target)	0.63 [0.37, 0.82]	12.0	0.028	0.65	0.43	-
Ensemble 2012-2025 (incl. training years)	0.62 [0.48, 0.78]	12.2	0.029	0.75	0.54	−0.01 [−0.12, +0.19]

Product	r [95 % CI]	n_{eff}	p (Dutilleul)	ρ	CSI top 20 %	Δr vs WGLC same period [95 % CI]
WGLC observed 2023-2025	0.46 [0.09, 0.76]	12.2	0.127	0.46	0.54	-
Ensemble 2023-2025 (test years)	0.53 [0.35, 0.71]	12.6	0.066	0.61	0.43	+0.07 [−0.13, +0.33]
U-Net / Attn U-Net / ConvLSTM / hybrid (test)	0.57 / 0.53 / 0.50 / 0.50	12-13	0.04-0.08	0.56-0.64	0.43-0.54	+0.04 to +0.11
CV-mosaic ensemble	0.31 [0.03, 0.53]	17.5	0.225	0.28	0.33	−0.33 [−0.74, +0.11]
Climatology (2012-2020)	0.66 [0.41, 0.84]	12.1	0.020	0.75	0.43	+0.03 [−0.03, +0.10]
CAPE × P proxy 2012-2025	0.05 [−0.39, 0.62]	15.8	0.865	0.15	0.11	−0.58 [−1.08, +0.05]

Chance-level CSI = 0.11. Satellite sampling-noise ceiling on attainable r: 0.997 (0.5°), 0.984 (5′). At 5′ (1,773 cells): WGLC r = 0.56, ensemble (test) 0.55, CV mosaic 0.23, proxy 0.13.

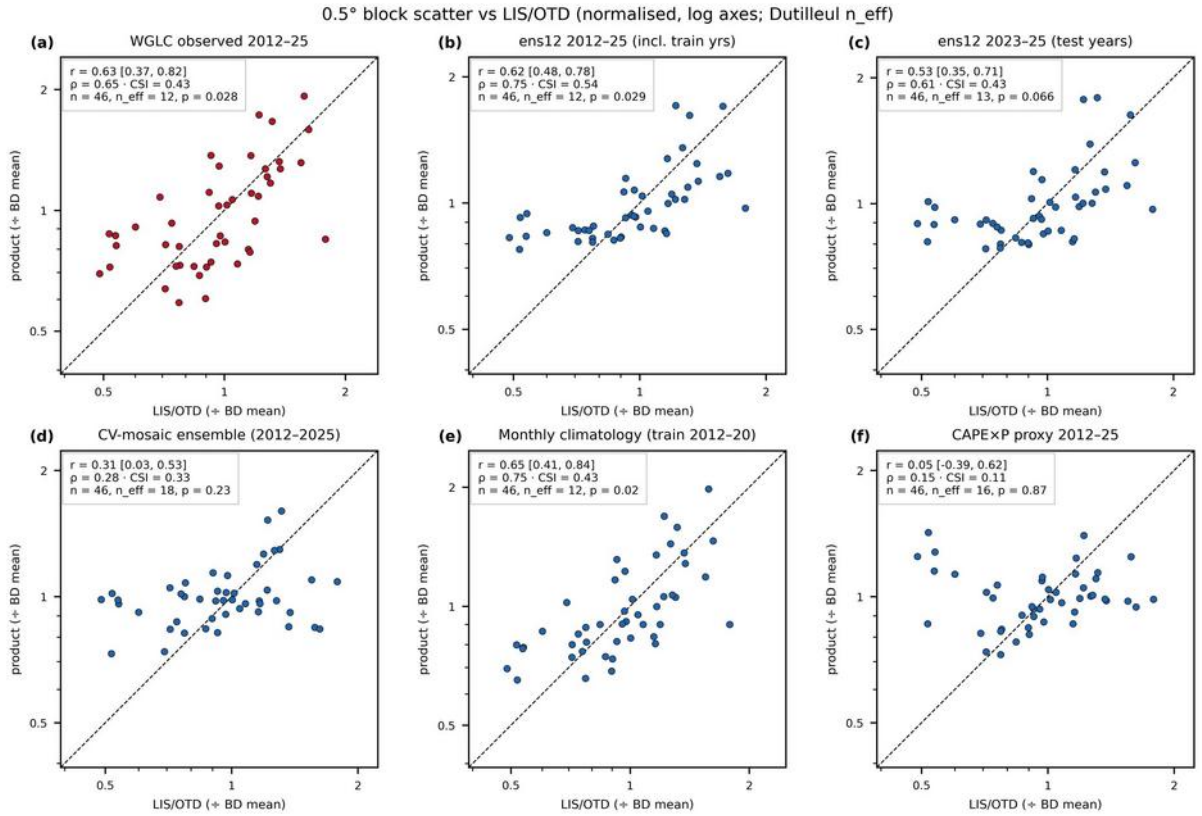


Figure 8. Independent validation on 46 exact 0.5° blocks, each product divided by its Bangladesh mean (log axes; dashed line 1:1): (a) WGLC 2012-2025; (b) ensemble 2012-2025; (c) ensemble

2023-2025; (d) spatial-CV mosaic; (e) climatology; (f) CAPE × P proxy. LIS/OTD on the axes denotes the satellite climatology (LIS/OTD Reprocessed Flash Climatology).

The remaining disagreement is structured (Appendix Figures B10, B11 and B14). Satellite sampling noise is negligible (noise ceiling 0.997; Appendix Figure B13), and agreement rises with smoothing (to r = 0.71 for WGLC and 0.67 for the ensemble at about 65 km), so the residual reflects a difference between the two records rather than model error. Relative to the satellite, WGLC has more lightning along the coast, in the south-east and in the north-eastern core, and less in the northern foothills and the west-center, with an implied strokes-per-flash ratio of 0.022 to 0.062 (10th to 90th percentile). Every product ranks the Sylhet region first (Appendix Table A4).

3.5 What drives the predictions

Integrated Gradients satisfied completeness closely (median relative error 0.09 %). For the national target, attribution was led by CAPE (14.3 ± 2.6 %) and CHIRPS rainfall (10.4 ± 1.7 %), followed by convective precipitation, AOD and the Total Totals index (Table 8; Figure 9). All 12 runs ranked CAPE first, agreement across runs was high (Kendall's W = 0.83, $p = 5 \times 10^{-27}$), and no static channel entered the top three, so the networks are unlikely to memorize location from static fields.

Table 8. Top-five predictors by Integrated-Gradients share of absolute attribution (%, mean over 12 runs; test months).

Target · season	Rank 1	Rank 2	Rank 3	Rank 4	Rank 5
Bangladesh · all months	CAPE 14.3 ± 2.6	CHIRPS 10.4 ± 1.7	CP 7.7 ± 1.8	AOD 7.6 ± 1.5	TT 6.6 ± 2.9
Bangladesh · MAM	CAPE 15.4 ± 3.6	AOD 11.5 ± 2.4	CP 7.6	CHIRPS 7.5	TT 7.5
Bangladesh · JJAS	CAPE 14.3	CHIRPS 10.5	WS 8.7	CP 6.9	AOD 6.2
Bangladesh · September	CAPE 17.5 ± 3.9	CHIRPS 13.0 ± 3.3	CP 6.7	D2M 6.4	WS 6.2
Bangladesh · ON	CHIRPS 13.1	CAPE 12.8	D2M 8.8	ELEV_SD 7.9	CP 6.6
Sylhet division (NE hotspot)	CHIRPS 14.3 ± 1.9	CAPE 12.5	WATER_FRAC 9.0	AOD 8.4	CP 7.0
Chittagong Hill Tracts	CAPE 13.9	CHIRPS 11.2	AOD 7.5	CP 7.2	NDVI 6.6

Target · season	Rank 1	Rank 2	Rank 3	Rank 4	Rank 5
Bangladesh · climatology baseline	CHIRPS 17.2	CP 13.1	AOD 12.1	CAPE 10.6	WS 8.0

Primary baseline: all-zero standardized input (2012-2020 mean state). Climatology baseline ranks dynamic channels only (static channels are zero by construction); its ranking correlates with the primary at Spearman 0.79.

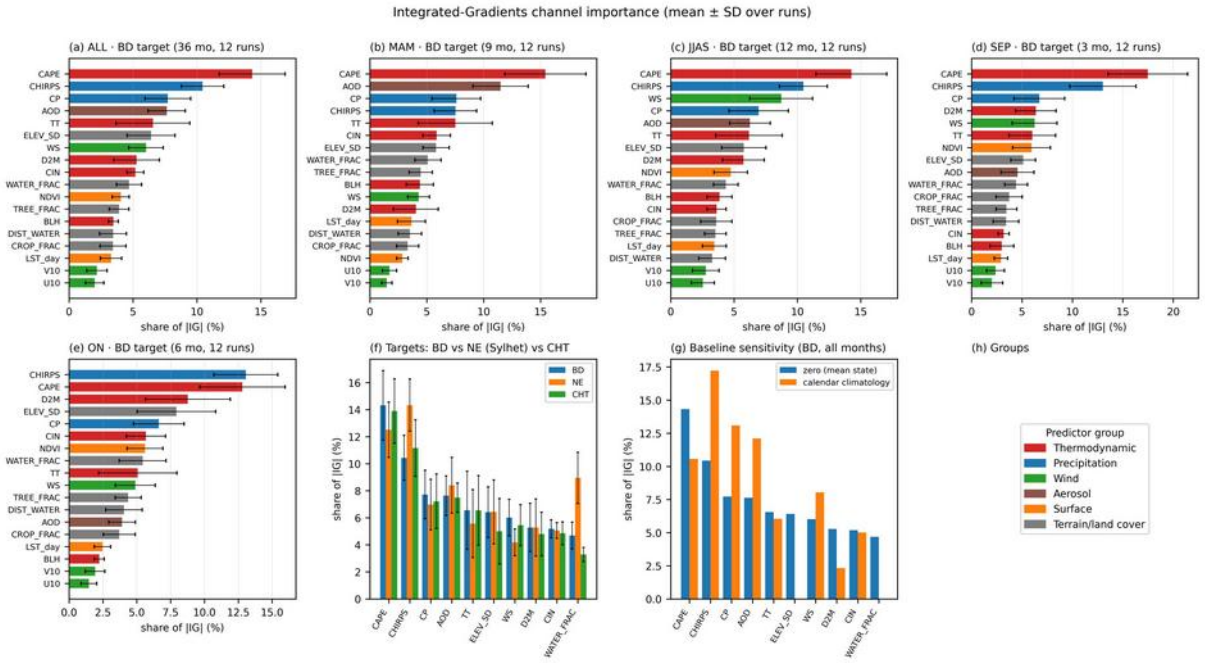


Figure 9. Integrated-Gradients channel importance (share of absolute attribution, mean ± SD over the 12 runs). (a) All test months, (b) MAM, (c) JJAS, (d) September and (e) ON for the Bangladesh target; (f) Bangladesh, Sylhet (NE) and CHT targets; (g) zero versus calendar-climatology baseline; (h) color key of predictor groups.

Drivers changed with season and region in physically sensible ways (Figure 10). In the pre-monsoon, AOD became the second input (11.5 %) and the dominant dynamic driver over 15 % of the country, mainly in the north-west. In ON, rainfall and dew point led, and over the Sylhet hotspot rainfall led with a 9 % contribution from wetland water fraction. The sequence models drew 41-59 % of their attribution from previous months (Appendix Figure B17a) yet were no more accurate than the U-Nets, so memory is used but adds little skill at the monthly scale.

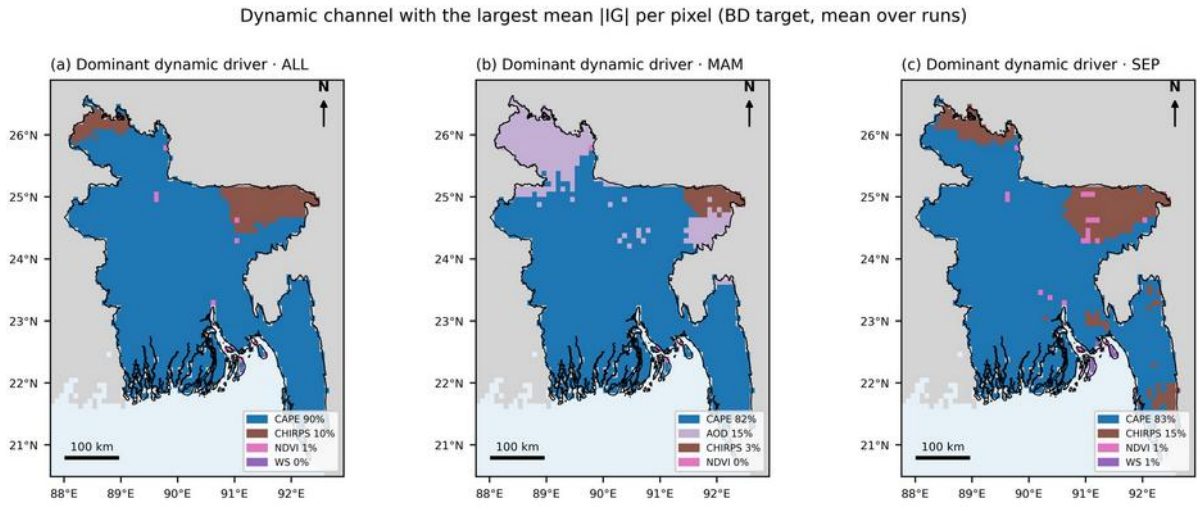


Figure 10. Dominant dynamic predictor per cell, i.e. the dynamic channel with the largest mean absolute IG (Bangladesh target, mean over runs): (a) all test months, (b) MAM and (c) September. Legend percentages give the share of Bangladesh cells.

Permutation importance agreed at the group level (Table 9; Appendix Figure B16). Permuting the precipitation group raised the test RMSE by 0.265 and the thermodynamic group by 0.105, whereas the other groups had small effects, and the permutation and IG rankings correlated at Spearman 0.72. Because the two methods order CAPE and CHIRPS differently, we interpret the result at the level of the instability-precipitation pair.

Table 9. Permutation importance on the test years (ensemble, inside Bangladesh; mean ± SD over five repeats).

Permuted unit	ΔRMSE	ΔCSI (loss)
Precipitation group (CP, CHIRPS)	+0.265 ± 0.019	+0.139
CHIRPS	+0.123 ± 0.032	+0.094
Thermodynamic group (CAPE, CIN, TT, D2M, BLH)	+0.105 ± 0.036	+0.109
CAPE	+0.094 ± 0.031	+0.091
CP	+0.055 ± 0.009	+0.068
ELEV_SD	+0.037 ± 0.007	−0.041
Terrain / land-cover group	+0.029	+0.009
Aerosol (AOD)	+0.011	+0.021
Surface group (LST day, NDVI)	+0.005	+0.006
Wind group (U10, V10, WS)	−0.002	−0.020

Baseline ensemble RMSE 0.596, CSI 0.273. Negative ΔCSI values reflect noise at the top-20 % threshold; ΔRMSE is the primary permutation metric. Dynamic maps were shuffled across months; static channels by 1° tiles.

3.6 A detection step in the record, and no detectable trend

The predefined test classified the WGLC record as detection-affected (Figure 11; Table 10). The annual observed density stepped up in 2016 (Pettitt $p = 0.026$; SNHT $p = 0.003$), from 0.81 to 1.59 strokes km^{-2} yr^{-1}, whereas CAPE, CHIRPS and CAPE × P showed no step near 2016. The ensemble stepped by a factor of only 1.38, reproducing about half of the observed log-step, possibly through dew point and wind anomalies that stepped at the same time. The residual step is consistent with the documented growth of WWLLN detection efficiency (Hutchins et al., 2012; Bürgesser, 2017).

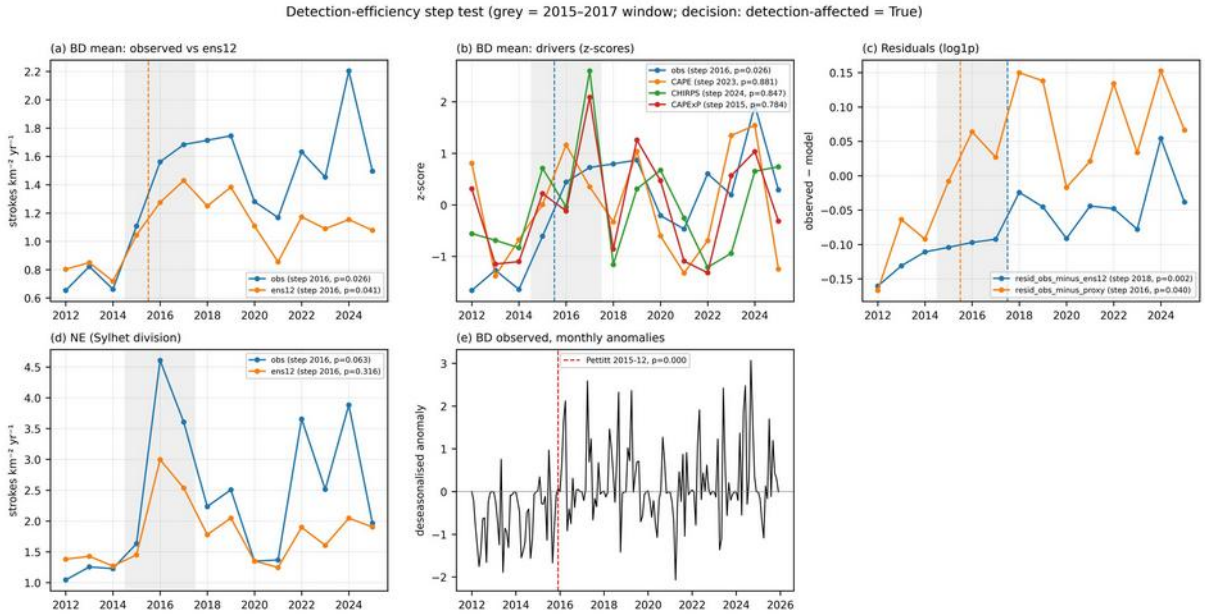


Figure 11. Detection-step test (grey band: the predefined 2015-2017 window; decision: detection-affected). (a) Annual Bangladesh-mean stroke density, observed and ensemble, with Pettitt step years; (b) standardized annual series of observations, CAPE, CHIRPS and CAPE × P; (c) residuals observed − ensemble and observed − proxy (log1p); (d) Sylhet division; (e) depersonalized monthly anomalies of the observed series with the Pettitt break.

Table 10. Change-point tests on annual Bangladesh-mean series and pixel-wise trends for the primary period 2016-2025.

Series	Pettitt step year (MC p)	SNHT year (p)	Before → after
Observed WGLC	2016 (0.026)	2016 (0.003)	0.81 → 1.59 (×1.96)

Series	Pettitt step year (MC p)	SNHT year (p)	Before → after
Ensemble	2016 (0.041)	2015 (0.020)	0.85 → 1.18 (×1.38)
CAPE	2023 (0.88)	2025 (0.92)	658 → 714 J kg^{-1}
CHIRPS	2024 (0.85)	2015 (0.77)	198 → 217 mm $month^{-1}$
CAPE × P	2015 (0.78)	2015 (0.88)	-
Residual observed − ensemble	2018 (0.002)	2018 (0.005)	−0.116 → −0.039
Residual observed − proxy	2016 (0.040)	2015 (0.011)	−0.083 → +0.077
Observed, Sylhet division	2016 (0.063)	2016 (0.16)	1.29 → 2.77 (×2.1)
Trends 2016-2025 (Mann-Kendall + Sen; BD-mean slope per year, MK p; field p)			
Observed · annual	−0.007 (p = 1.00)	field p = 0.87	FDR-significant cells: 0 %
Observed · MAM	−0.072 (p = 0.11)	field p = 0.07	0 %
Observed · JJAS	+0.105 (p = 0.11)	field p = 0.18	0 %
Observed · September	+0.174 (p = 0.37)	field p = 0.06	0 %
Ensemble · annual	−0.027 (p = 0.03)	field p = 0.32	0 %
Sensitivity 2012-2025 · observed annual / JJAS	+0.074 (p = 0.021) / +0.158 (p = 0.001)	field p = 0.007 / 0.001	0 % (ensemble +0.018, p = 0.44)

Densities in strokes km^{-2} yr^{-1}. Decision rule fixed before analysis: an observed step beginning 2015-2017 with $p < 0.05$, absent (±1 yr) from CAPE, CHIRPS and CAPE × P → detection-affected → trends restricted to 2016-2025.

Over 2016-2025, no cell had a significant trend after false-discovery-rate control, in any season, for the observations or the ensemble (Table 10; Appendix Figures B18 and B19). Over 2012-2025, the observed annual, monsoon and September series would appear to increase significantly, but the ensemble does not reproduce these increases, which are largely an artefact of the detection step. We therefore make no claim of increasing lightning.

3.7 Lightning risk: a robust top and an uncertain middle

The 2016-2025 ensemble hazard averaged 1.18 strokes km^{-2} yr^{-1}, about 26 % below observed WGLC, but its spatial pattern correlated at 0.88 with the observed map (Appendix Figure B21). Exposure and vulnerability were strongly anti-correlated (Spearman −0.78), whereas hazard was nearly independent of both.

Risk concentrates in the north-eastern haor basin and along the Meghalaya foothills (Figure 12; Table 11). All ten highest-ranked upazilas lie in Sunamganj and Sylhet districts, led by Tahirpur, Dakshin Sunamganj, Jaintiapur and Gowainghat, and 35 of the top 50 are in Sylhet division (Appendix Table A7). Sylhet's mean risk (0.379) is twice that of Mymensingh (0.183), while dense cities fall into the lowest class because of their low vulnerability index. Separately, 50 upazilas, home to 15.5 million people, have a probability of at least 0.9 of being high or very high risk. This set overlaps with the top 50 by risk (47 of the 50) but is not identical to it.

Table 11. Regional summary of upazila-level risk (primary annual risk, 2016-2025 hazard).

Region	Units (upazila, GADM L3)	Population 2025 (M)	Area-weighted mean risk	Very-high upazilas	Top-50 upazilas
Sylhet	38	12.8	0.379	38	35
Mymensingh	34	13.3	0.183	20	9
Rangpur	58	18.1	0.129	23	1
CHT hills	25	2.1	0.104	10	1
Chittagong	86	30.0	0.095	6	0
Dhaka	130	51.3	0.092	12	4
Barisal	40	7.6	0.074	0	0
Rajshahi	70	21.4	0.068	0	0
Khulna	64	16.6	0.040	0	0

The CHT hills (Rangamati, Khagrachhari, Bandarban) are shown separately from Chittagong division.

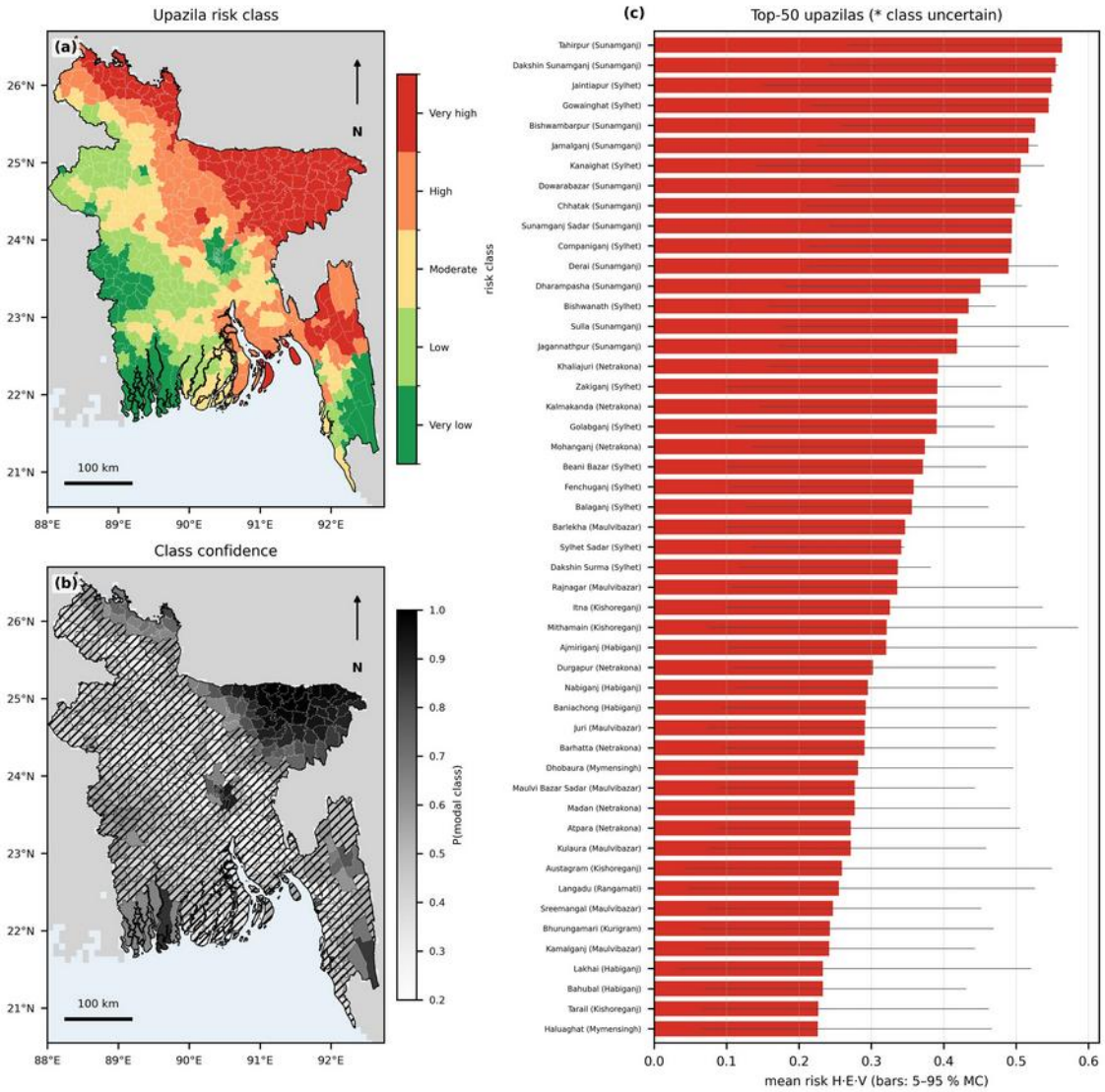


Figure 12. Upazila-level lightning risk, the main product. (a) Quintile classes of area-weighted mean risk R = H·E·V; (b) Monte-Carlo probability of the modal class with spatially coherent hazard errors (hatched: < 0.60, class uncertain); (c) top-50 upazilas with 5-95 % Monte-Carlo intervals (none has an uncertain class). Pixel-level risk, confidence and P(high or very high) are shown in Appendix Figure B22.

The top of the ranking is robust to hazard uncertainty, but the middle is not. The calibrated error correlation gave 86 % coverage of the 2023-2025 mean map at the nominal 90 % level. None of the top-50 upazilas had an uncertain class (modal-class probabilities 0.78-1.00), whereas 388 of the 545 upazilas (GADM level-3 units; Section 2.1) did, so adjacent middle classes cannot be distinguished.

3.8 Sensitivity of the ranking and the satellite hazard

The ranking was stable under alternative weights, hazard periods, scaling and exposure and vulnerability definitions (Spearman 0.87-1.00; 45-50 of the top 50 retained; Table 12; Appendix Figure B23). Dropping vulnerability changed it markedly (ρ = 0.49), because E and V are anti-correlated. With the observed WGLC hazard, ρ was 0.89 and 40 of the top 50 were retained; with the satellite hazard, ρ was 0.75 and 55 % of upazilas changed class.

Table 12. Sensitivity of the upazila risk ranking to alternative formulations (vs the primary ranking).

Variant	Spearman ρ	Top-50 overlap	Upazilas changing class (%)
Weights: H 0.50 / E 0.50 / V 0.50 / H 0.60	0.966 / 0.986 / 0.949 / 0.874	49 / 49 / 45 / 48	20 / 13 / 30 / 40
Hazard 2012-2025	0.994	49	10
Hazard log-scaled	1.000	49	1
Hazard = observed WGLC 2016-2025	0.887	40	43
Hazard = satellite TRMM-LIS/ISS-LIS	0.745	26	55
Exposure POP 2020 / POP × cropland / POP & built-up	1.000 / 0.984 / 0.959	50 / 47 / 45	1 / 12 / 27
Vulnerability NTL only / access only	0.972 / 0.978	45 / 47	18 / 19
No vulnerability (H × E)	0.486	46	60

The satellite hazard alters the middle of the ranking but leaves the top largely intact, with 49 of the primary top 50 still high or very high (Figure 13). It raises the west-center and north-west and lowers the coast, following the record differences in Section 3.4. Because quintiles are ranks, these shifts are zero-sum.

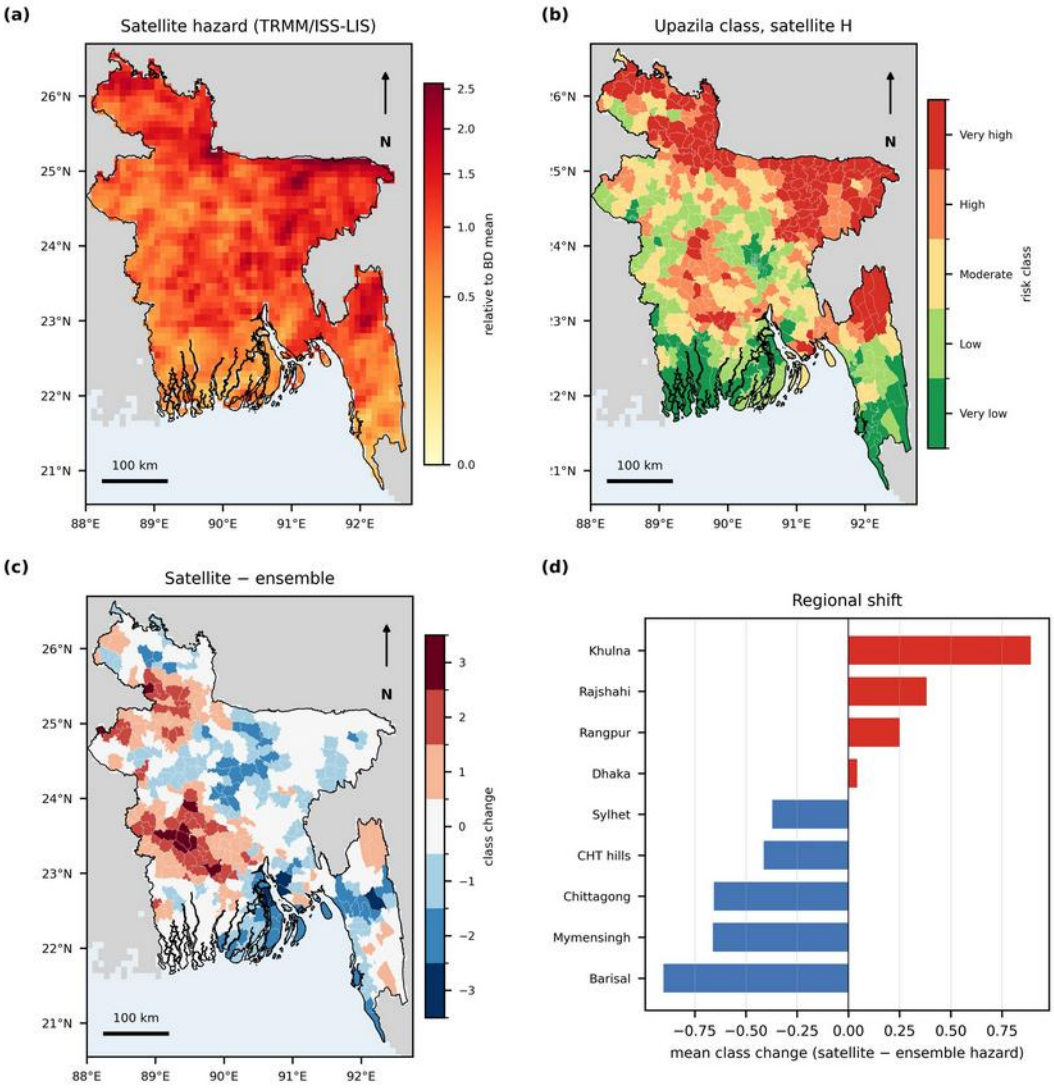


Figure 13. Risk with the independent satellite climatology as hazard. (a) TRMM-LIS/ISS-LIS flash density relative to its Bangladesh mean; (b) upazila risk classes with the satellite hazard; (c) class change (satellite − ensemble hazard); (d) population-weighted mean class change by region.

3.9 Seasonal risk and fatalities

Pre-monsoon risk is closest to the annual ranking (ρ = 0.86) and is led by upazilas on the Meghalaya foothills, monsoon risk shifts towards the Sunamganj haor, and September risk brings Langadu in Rangamati into the top three (Appendix Table A6; Figure B24).

District deaths for 2015-2022 agreed only weakly with the primary annual risk (Spearman ρ = 0.19 per area, p = 0.13; 0.19 per capita, p = 0.14; Figure 14; Table 13). The strongest association per area came from risk built on the pre-monsoon hazard (ρ = 0.40, p = 0.001), which survives a Bonferroni

correction across the 26 layers, and the strongest per-capita association from risk built on the satellite hazard (ρ = 0.34, p = 0.006). The ensemble hazard related to deaths more closely than the observed WGLC hazard (annual risk ρ = 0.19 against 0.09). Vulnerability was positively (ρ = 0.31) and exposure negatively (ρ = −0.33) related to per-capita deaths, so rural and remote districts have higher death rates.

Table 13. Spearman correlation between district mean risk or hazard and lightning deaths, 2015-2022 (n = 64 districts; selected layers of 26).

Layer	ρ, deaths per 1,000 km² (p)	ρ, deaths per million (p)
Risk with MAM hazard	0.404 (0.001)	0.208 (0.10)
MAM ensemble hazard alone	0.372 (0.002)	−0.051 (0.69)
Risk with satellite hazard	0.326 (0.009)	0.340 (0.006)
Satellite hazard alone	0.325 (0.009)	0.101 (0.42)
Exposure alone (E)	0.310 (0.013)	−0.325 (0.009)
Risk with JJAS hazard	0.196 (0.12)	0.329 (0.008)
Primary risk (annual ensemble H·E·V)	0.191 (0.13)	0.185 (0.14)
Annual ensemble hazard alone	0.152 (0.23)	−0.018 (0.89)
Risk with observed WGLC hazard	0.086 (0.50)	0.084 (0.51)
Observed WGLC hazard alone	0.040 (0.75)	−0.098 (0.44)
Vulnerability alone (V)	−0.252 (0.045)	0.308 (0.013)

p-values ignore spatial autocorrelation; with 26 layers tested, results are exploratory (Bonferroni threshold 0.0019). Deaths from Ahmed et al. (2024), 2,142 deaths in total.

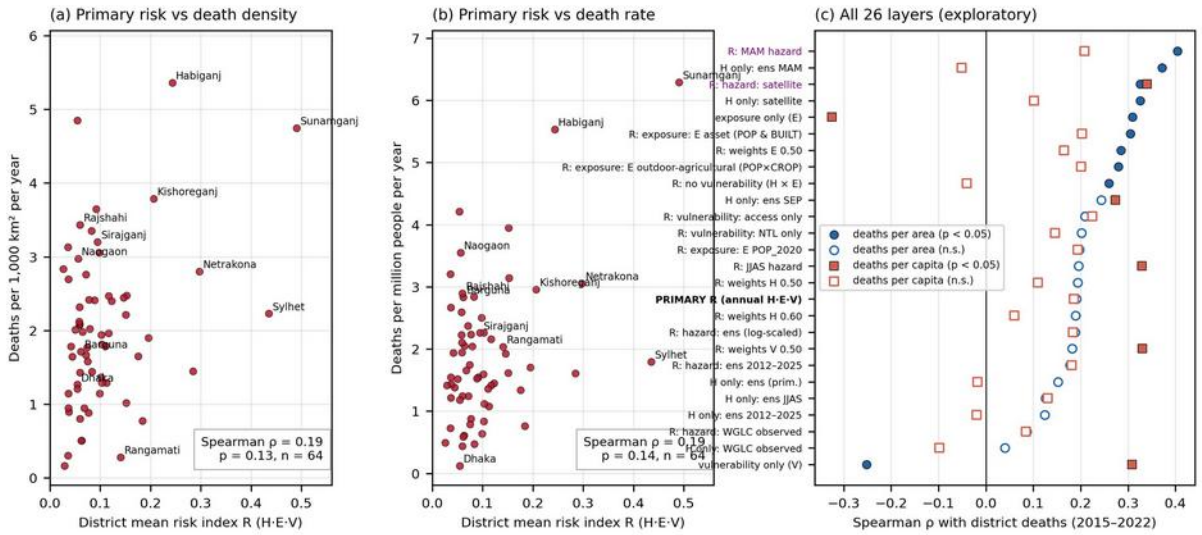


Figure 14. Fatality check. District mean primary risk against (a) deaths per 1,000 km² per year and (b) deaths per million people per year, 2015-2022 (Ahmed et al., 2024). (c) Spearman ρ between district deaths and all 26 risk and hazard layers; filled markers $p < 0.05$ (uncorrected); pre-monsoon (MAM) and satellite-hazard risk highlighted.

4. Discussion

Deep learning added skill to national lightning hazard mapping, but not everywhere one might expect. Every architecture beat monthly climatology on unseen years, yet a two-variable proxy came close on bulk RMSE, echoing the success of CAPE × precipitation as a lightning parameterization (Romps et al., 2014) and the strong CAPE-lightning coupling in Bangladesh (Dewan et al., 2018a). The added value of the networks is spatial: they reproduced the organization of lightning (pattern *r* 0.70 against 0.43; hotspot CSI 0.27 against 0.08) and agreed with the satellite record where the proxy did not. The proxy predicts how much convection a month carries, whereas the networks, reading terrain, land cover, moisture and aerosol in context, predict *where* that convection produces lightning, which is what hazard mapping needs.

This advantage did not depend on network design. The four architectures were statistically tied, and the sequence models used temporal memory without gaining accuracy, which suggests that at a monthly scale antecedent conditions add little beyond the current month's thermodynamics and rainfall. Compact models therefore suffice, ensembles are more valuable than architectural novelty, and the training objective matters more than the architecture, since the hotspot-weighted loss gave the clearest gain. The significance tests add a caveat: month by month the models did not place hotspots better than climatology, and persistence did better, so the pooled gain comes from

knowing which months are active. This distinction is easy to miss when only pooled scores are reported.

The attributions are consistent with the physics of tropical lightning (Williams, 2005): instability and precipitation led in every architecture, season and region, and the rankings were consistent across runs. Because consistency is not proof of correctness, we also checked whether the seasonal and regional variations made sense (McGovern et al., 2019; Mamalakis et al., 2022). AOD rose in the pre-monsoon and in the north-west, where transported dust and sulphate peak and where recent work links aerosol to the primary lightning maximum (Azam et al., 2026). Aerosol invigoration of convection is plausible (Rosenfeld et al., 2008; Yuan et al., 2011; Thornton et al., 2017), but AOD also tracks the pre-monsoon thermodynamic regime (Rafiuddin et al., 2025), so the attribution shows that the model uses AOD, not that aerosol causes lightning. The precipitation-led north-eastern hotspot is consistent with orographic convection over the moist haor basin, and the post-monsoon regime with convection that becomes moisture-limited as instability declines.

The validation also shows that the ground-based and satellite records agree on national geography but not on every detail. Outside the north-east, WGLC is relatively higher along the coast and lower in the northern foothills and the west-centre. Regional variation in WWLLN detection efficiency (Rodger et al., 2006; Hutchins et al., 2012), in the intra-cloud share of lightning and in the periods covered can all contribute, whereas satellite sampling noise can be ruled out. Our models inherit the geography of WGLC and cannot be expected to agree with an independent reference much better than their training target, and they did not.

The 2016 step is the more consequential finding for users of the record. A near doubling of stroke density that no physical driver shares is consistent with WWLLN network growth (Hutchins et al., 2012; Bürgesser, 2017; Kaplan and Lau, 2021). Without the test, the full record would have suggested significant increases in lightning, a claim that recurs in public debate; after the step, no cell shows a trend, in line with the view that rising fatalities reflect growing exposure more than a changing hazard (Mongabay, 2026). The models also reproduced about half of the step from inputs that happened to step at the same time, a subtle learned artefact. Homogeneity tests should therefore precede any trend or attribution study based on gridded lightning records.

These detection problems also explain why the risk analysis uses the modelled hazard even though WGLC covers every cell. The ensemble expresses hazard as a function of physical drivers, which

limits the transfer of network artefacts; it agreed with the satellite climatology at least as well as the observations on the test years (r = 0.53 against 0.46), related more closely to district deaths (ρ = 0.19 against 0.09) and supplies a calibrated uncertainty that can be propagated to the ranking. The choice does not drive the main conclusions, since the observed-hazard ranking correlates with the primary one at ρ = 0.89.

The risk map places the national priority clearly. The north-eastern haor basin and the Meghalaya foothills combine the highest hazard with a large, rural and poorly served population, and this top of the ranking holds under hazard uncertainty, alternative formulations and an independent hazard record. The actionable result is that 50 upazilas with 15.5 million people have at least 90 % probability of being high or very high risk. This matches the fatality geography, in which Sunamganj has the highest per-capita death rate (Ahmed et al., 2024), and the priorities of district vulnerability studies (Mazumder and Saroar, 2025).

The middle of the ranking is not robust. Two-thirds of upazilas have uncertain classes, and outside the north-east the ranking depends on the lightning record, particularly in the west-center and north-west, where WWLLN appears to under-detect. Several high-fatality districts (Naogaon, Rajshahi, Chapai Nawabganj and Sirajganj) lie there, and risk built on the satellite hazard gave the only clear per-capita association. Rankings outside the north-east should therefore be read as indicative until detection efficiency is better characterized.

The stronger link of deaths with pre-monsoon than with annual risk (ρ = 0.40 against 0.19) is a lesson about timing. The annual hazard is dominated by September, whereas deaths concentrate in April-May, when Nor'westers coincide with the *boro* harvest and many people work in exposed fields (Holle et al., 2019; Dewan et al., 2017). Risk therefore depends on *when* people are outside as well as on where lightning strikes, and a national product for warnings or shelter placement should be seasonal and weighted by the agricultural calendar. Practical measures follow directly: lightning-safe shelters and arresters in the haor fields and warnings timed to the harvest (Cooper and Holle, 2019).

Several limitations bound these conclusions. WGLC inherits WWLLN detection efficiency, which varies in space and time, so absolute densities are relative and a decade of post-step data cannot support trends. The models compress spatial contrasts, underpredict the September maximum of the south-eastern hills and transfer weakly in space, and the calibrated uncertainty relies on one

factor fitted on validation years that were also used for early stopping. Some inputs required gap filling or substitution, and CHIRPS contains a product discontinuity near 91.5°E. The satellite comparison rests on an effective sample of about 12, the attributions explain the model rather than the atmosphere, the risk index involves subjective choices and proxy-based vulnerability, and the fatality data are incomplete and cover only 64 districts.

These limitations indicate where the framework can go next: regional detection-efficiency corrections or multi-source targets that combine WGLC with satellite and national networks, sub-seasonal targets aligned with the agricultural calendar, and spatially explicit fatality models with upazila casualty data. The data cube design, the predefined rules, the independent validation and the uncertainty-aware ranking can be applied unchanged to other lightning-prone countries in South Asia and Africa.

5. Conclusion

This study developed a raster-native deep-learning framework for national lightning hazard and risk mapping in Bangladesh and evaluated it against simple baselines, an independent satellite record and observed fatalities. Image-to-image networks reproduced monthly stroke density on unseen years better than climatology, reducing the mean squared error by a fifth and nearly doubling the pooled hotspot critical success index, although the four architectures were statistically indistinguishable. A simple CAPE × precipitation proxy matched the networks on bulk error but failed on spatial pattern, hotspots and independent validation, which shows that the real contribution of deep learning lies in locating where convection produces lightning rather than in estimating how much convection occurs. The learned hazard agreed with the TRMM-LIS/ISS-LIS climatology as well as its own training record did, and its explanations were physically plausible and consistent across architectures.

The study also shows why lightning records must be tested before they are used for policy. The WWLLN-based record contains a 2016 detection step that no physical driver shares, and once this step is accounted for, no significant lightning trend remains. Combining the hazard with exposure and vulnerability places the national priority clearly in the north-eastern haor basin, where 50 upazilas with 15.5 million people are high or very high risk with at least 90 % probability. The middle of the ranking remains uncertain, however, and deaths follow pre-monsoon risk more closely than annual risk, pointing to exposure during the harvest season. Shelters, arresters and

harvest-timed warnings should therefore be concentrated in the haor belt now, while rankings elsewhere are refined with better lightning observations and casualty data.

These findings directly support the Sustainable Development Goals. By identifying where and when rural people are most exposed, the framework contributes to SDG 13 (Climate Action), particularly Target 13.1 on strengthening resilience and adaptive capacity to climate-related hazards. By providing a transparent, uncertainty-aware basis for early warning and shelter placement, it supports SDG 11 (Sustainable Cities and Communities), Target 11.5, which seeks to reduce deaths caused by disasters. Because most victims are poor farmers and fishers working in open fields, targeted protection in high-risk upazilas also advances SDG 1 (No Poverty), Target 1.5, by reducing the exposure of vulnerable communities to climate-related extreme events.

What's Next

Bangladesh can now see, upazila by upazila, where lightning is most likely to harm people and how certain that picture is. The clearest message is that the north-eastern haor basin should be protected first, through lightning-safe shelters in open paddy fields and wetlands, simple warnings timed to the boro harvest in April-May, and awareness work with farmers and fishers. Because the maps carry their own uncertainty, planners can act firmly where the evidence is strong and wait for better information where it is not, instead of spreading scarce resources evenly.

Three steps would make the next generation of maps more useful. First, longer and more consistent lightning observations, including continued satellite records and a ground network inside Bangladesh, would separate real changes in lightning from changes in the instruments that record it. Second, casualty records at upazila level, noting where people were and what they were doing when struck, would allow risk maps to be tested at the scale where decisions are made. Third, linking the framework to short-range weather forecasts could turn a static hazard map into a season-aware warning service. Other lightning-prone and data-poor countries in South Asia and the tropics face the same problems, and the approach could be adapted to them.

CRediT authorship contribution statement

Fardin Bin Faruque: Conceptualization, Methodology, Software, Formal analysis, Writing – original draft.

Kazi Tahmid Parveg: Data curation, Validation, Writing – review & editing.

Jannatul Ferdous: Investigation, Visualization, Writing – review & editing.

Declaration of competing interest

The authors declare that they have no known competing financial interests or personal relationships that could have appeared to influence the work reported in this paper.

Funding

This research did not receive any specific grant from funding agencies in the public, commercial, or not-for-profit sectors.

Ethics statement

Not applicable. This study used only publicly available gridded datasets and published, district-level aggregated fatality counts; it did not involve human participants, personal data or animals.

Declaration of generative AI and AI-assisted technologies in the manuscript preparation process

During the preparation of this manuscript, the authors used Claude (Anthropic) to improve the language, clarity, readability and formatting of the text, and to help adapt the title, abstract, highlights and What's Next section to the journal's format. Following the use of this tool, the authors carefully reviewed and edited all outputs to ensure accuracy, scientific integrity and alignment with the study's original findings. The authors take full responsibility for the content of this publication. Generative AI was not used for any aspect of the research design, data collection, data analysis, results interpretation or the formulation of conclusions. No AI-generated images, figures or tables are included in this manuscript.

Data availability

The data and code that support the findings of this study will be made available by the corresponding author on reasonable request.

References

Ahmed, F., Hasan, S., Mahbubul, I.M., Mallik, M.A.K., Hossen, M.N., 2024. GIS-based spatial analysis for lightning scenario in Bangladesh. Heliyon 10(7), e28708. https://doi.org/10.1016/j.heliyon.2024.e28708

Albrecht, R.I., Goodman, S.J., Buechler, D.E., Blakeslee, R.J., Christian, H.J., 2016. Where are the lightning hotspots on Earth? Bull. Am. Meteorol. Soc. 97, 2051-2068. https://doi.org/10.1175/BAMS-D-14-00193.1

Alexandersson, H., 1986. A homogeneity test applied to precipitation data. J. Climatol. 6, 661-675. https://doi.org/10.1002/joc.3370060607

Azam, A.T.M.S., Akter, N., Dewan, A., Molla, M.A.-M., Rafiuddin, M., 2026. Role of pollutants on the bimodal lightning distribution in Bangladesh. Earth Syst. Environ. 10, 663-678. https://doi.org/10.1007/s41748-025-00627-w

Barlow, R.E., Bartholomew, D.J., Bremner, J.M., Brunk, H.D., 1972. Statistical Inference under Order Restrictions. Wiley, New York.

Benjamini, Y., Hochberg, Y., 1995. Controlling the false discovery rate: a practical and powerful approach to multiple testing. J. R. Stat. Soc. B 57, 289-300. https://doi.org/10.1111/j.2517-6161.1995.tb02031.x

Blakeslee, R.J., Lang, T.J., Koshak, W.J., Buechler, D., Gatlin, P., Mach, D.M., Stano, G.T., Virts, K.S., Walker, T.D., Cecil, D.J., Ellett, W., Goodman, S.J., Harrison, S., Hawkins, D.L., Heumesser, M., Lin, H., Maskey, M., Schultz, C.J., Stewart, M., Bateman, M., Chanrion, O., Christian, H., 2020. Three years of the Lightning Imaging Sensor onboard the International Space Station: expanded global coverage and enhanced applications. J. Geophys. Res. Atmos. 125, e2020JD032918. https://doi.org/10.1029/2020JD032918

Breiman, L., 2001. Random forests. Mach. Learn. 45, 5-32. https://doi.org/10.1023/A:1010933404324

Buchhorn, M., Lesiv, M., Tsendbazar, N.-E., Herold, M., Bertels, L., Smets, B., 2020. Copernicus Global Land Cover Layers: Collection 2. Remote Sens. 12, 1044. https://doi.org/10.3390/rs12061044

Bürgesser, R.E., 2017. Assessment of the World Wide Lightning Location Network (WWLLN) detection efficiency by comparison to the Lightning Imaging Sensor (LIS). Q. J. R. Meteorol. Soc. 143, 2809-2817. https://doi.org/10.1002/qj.3129

Cardona, O.D., van Aalst, M.K., Birkmann, J., Fordham, M., McGregor, G., Perez, R., Pulwarty, R.S., Schipper, E.L.F., Sinh, B.T., 2012. Determinants of risk: exposure and vulnerability, in: Field, C.B., Barros, V., Stocker, T.F., Qin, D., Dokken, D.J., Ebi, K.L., Mastrandrea, M.D., Mach, K.J., Plattner, G.-K., Allen, S.K., Tignor, M., Midgley, P.M. (Eds.), Managing the Risks of Extreme Events and Disasters to Advance Climate Change Adaptation (SREX). Cambridge University Press, Cambridge, pp. 65-108.

Cecil, D.J., Buechler, D.E., Blakeslee, R.J., 2014. Gridded lightning climatology from TRMM-LIS and OTD: dataset description. Atmos. Res. 135-136, 404-414. https://doi.org/10.1016/j.atmosres.2012.06.028

Christian, H.J., Blakeslee, R.J., Boccippio, D.J., Boeck, W.L., Buechler, D.E., Driscoll, K.T., Goodman, S.J., Hall, J.M., Koshak, W.J., Mach, D.M., Stewart, M.F., 2003. Global frequency and distribution of lightning as observed from space by the Optical Transient Detector. J. Geophys. Res. 108(D1), 4005. https://doi.org/10.1029/2002JD002347

Clifford, P., Richardson, S., Hémon, D., 1989. Assessing the significance of the correlation between two spatial processes. Biometrics 45, 123-134. https://doi.org/10.2307/2532039

Cooper, M.A., Holle, R.L., 2019. Reducing Lightning Injuries Worldwide. Springer Natural Hazards, Springer, Cham. https://doi.org/10.1007/978-3-319-77563-0

Crichton, D., 1999. The risk triangle, in: Ingleton, J. (Ed.), Natural Disaster Management. Tudor Rose, London, pp. 102-103.

Dewan, A., Hossain, M.F., Rahman, M.M., Yamane, Y., Holle, R.L., 2017. Recent lightning-related fatalities and injuries in Bangladesh. Weather Clim. Soc. 9, 575-589. https://doi.org/10.1175/WCAS-D-16-0128.1

Dewan, A., Ongee, E.T., Rafiuddin, M., Rahman, M.M., Mahmood, R., 2018a. Lightning activity associated with precipitation and CAPE over Bangladesh. Int. J. Climatol. 38, 1649-1660. https://doi.org/10.1002/joc.5286

Dewan, A., Ongee, E.T., Rahman, M.M., Mahmood, R., Yamane, Y., 2018b. Spatial and temporal analysis of a 17-year lightning climatology over Bangladesh with LIS data. Theor. Appl. Climatol. 134, 347-362. https://doi.org/10.1007/s00704-017-2278-3

Didan, K., 2015. MOD13A3 MODIS/Terra Vegetation Indices Monthly L3 Global 1km SIN Grid V006. NASA EOSDIS Land Processes DAAC. https://doi.org/10.5067/MODIS/MOD13A3.006

Dutilleul, P., 1993. Modifying the t test for assessing the correlation between two spatial processes. Biometrics 49, 305-314. https://doi.org/10.2307/2532625

Elvidge, C.D., Zhizhin, M., Ghosh, T., Hsu, F.-C., Taneja, J., 2021. Annual time series of global VIIRS nighttime lights derived from monthly averages: 2012 to 2019. Remote Sens. 13, 922. https://doi.org/10.3390/rs13050922

Farukh, M.A., Ahmed, S.U., Islam, M.A., Baten, M.A., 2017. Spatial vulnerability assessment of extreme lightning events in Bangladesh using GIS. J. Environ. Sci. Nat. Resour. 10(2), 11-18. https://doi.org/10.3329/jesnr.v10i2.39008

Fortin, V., Abaza, M., Anctil, F., Turcotte, R., 2014. Why should ensemble spread match the RMSE of the ensemble mean? J. Hydrometeorol. 15, 1708-1713. https://doi.org/10.1175/JHM-D-14-0008.1

Funk, C., Peterson, P., Landsfeld, M., Pedreros, D., Verdin, J., Shukla, S., Husak, G., Rowland, J., Harrison, L., Hoell, A., Michaelsen, J., 2015. The climate hazards infrared precipitation with stations: a new environmental record for monitoring extremes. Sci. Data 2, 150066. https://doi.org/10.1038/sdata.2015.66

GADM, 2022. GADM database of Global Administrative Areas, version 4.1. https://gadm.org

Gal, Y., Ghahramani, Z., 2016. Dropout as a Bayesian approximation: representing model uncertainty in deep learning. Proc. 33rd Int. Conf. Mach. Learn. (ICML), PMLR 48, 1050-1059.

Gelaro, R., McCarty, W., Suárez, M.J., Todling, R., Molod, A., Takacs, L., Randles, C.A., Darmenov, A., Bosilovich, M.G., Reichle, R., Wargan, K., Coy, L., Cullather, R., Draper, C., Akella, S., Buchard, V., Conaty, A., da Silva, A.M., Gu, W., Kim, G.-K., Koster, R., Lucchesi, R., Merkova, D., Nielsen, J.E., Partyka, G., Pawson, S., Putman, W., Rienecker, M., Schubert, S.D., Sienkiewicz, M., Zhao, B., 2017. The Modern-Era Retrospective Analysis for Research and Applications, version 2 (MERRA-2). J. Clim. 30, 5419-5454. https://doi.org/10.1175/JCLI-D-16-0758.1

Geng, Y., Li, Q., Lin, T., Jiang, L., Xu, L., Zheng, D., Yao, W., Lyu, W., Zhang, Y., 2019. LightNet: a dual spatiotemporal encoder network model for lightning prediction. Proc. 25th ACM SIGKDD Int. Conf. Knowl. Discov. Data Min., 2439-2447. https://doi.org/10.1145/3292500.3330717

Gneiting, T., Raftery, A.E., 2007. Strictly proper scoring rules, prediction, and estimation. J. Am. Stat. Assoc. 102, 359-378. https://doi.org/10.1198/016214506000001437

Hersbach, H., Bell, B., Berrisford, P., Hirahara, S., Horányi, A., Muñoz-Sabater, J., Nicolas, J., Peubey, C., Radu, R., Schepers, D., Simmons, A., Soci, C., Abdalla, S., Abellan, X., Balsamo, G., Bechtold, P., Biavati, G., Bidlot, J., Bonavita, M., De Chiara, G., Dahlgren, P., Dee, D., Diamantakis, M., Dragani, R., Flemming, J., Forbes, R., Fuentes, M., Geer, A., Haimberger, L., Healy, S., Hogan, R.J., Hólm, E., Janisková, M., Keeley, S., Laloyaux, P., Lopez, P., Lupu, C., Radnoti, G., de Rosnay, P., Rozum, I., Vamborg, F., Villaume, S., Thépaut, J.-N., 2020. The ERA5 global reanalysis. Q. J. R. Meteorol. Soc. 146, 1999-2049. https://doi.org/10.1002/qj.3803

Holle, R.L., 2016. A summary of recent national-scale lightning fatality studies. Weather Clim. Soc. 8, 35-42. https://doi.org/10.1175/WCAS-D-15-0032.1

Holle, R.L., Dewan, A., Said, R., Brooks, W.A., Hossain, M.F., Rafiuddin, M., 2019. Fatalities related to lightning occurrence and agriculture in Bangladesh. Int. J. Disaster Risk Reduct. 41, 101264. https://doi.org/10.1016/j.ijdrr.2019.101264

Holm, S., 1979. A simple sequentially rejective multiple test procedure. Scand. J. Stat. 6, 65-70.

Hutchins, M.L., Holzworth, R.H., Brundell, J.B., Rodger, C.J., 2012. Relative detection efficiency of the World Wide Lightning Location Network. Radio Sci. 47, RS6005. https://doi.org/10.1029/2012RS005049

Jarvis, A., Reuter, H.I., Nelson, A., Guevara, E., 2008. Hole-filled SRTM for the globe, version 4. CGIAR-CSI SRTM 90 m Database. https://srtm.csi.cgiar.org

Jenks, G.F., 1967. The data model concept in statistical mapping. Int. Yearb. Cartogr. 7, 186-190.

Kaplan, J.O., Lau, K.H.-K., 2021. The WGLC global gridded lightning climatology and time series. Earth Syst. Sci. Data 13, 3219-3237. https://doi.org/10.5194/essd-13-3219-2021

Kendall, M.G., 1975. Rank Correlation Methods, 4th ed. Charles Griffin, London.

Kendall, M.G., Babington Smith, B., 1939. The problem of m rankings. Ann. Math. Stat. 10, 275-287. https://doi.org/10.1214/aoms/1177732186

Künsch, H.R., 1989. The jackknife and the bootstrap for general stationary observations. Ann. Stat. 17, 1217-1241. https://doi.org/10.1214/aos/1176347265

Lakshminarayanan, B., Pritzel, A., Blundell, C., 2017. Simple and scalable predictive uncertainty estimation using deep ensembles. Adv. Neural Inf. Process. Syst. 30, 6402-6413.

Leinonen, J., Hamann, U., Germann, U., 2022. Seamless lightning nowcasting with recurrent-convolutional deep learning. Artif. Intell. Earth Syst. 1, e220043. https://doi.org/10.1175/AIES-D-22-0043.1

Livezey, R.E., Chen, W.Y., 1983. Statistical field significance and its determination by Monte Carlo techniques. Mon. Weather Rev. 111, 46-59. https://doi.org/10.1175/1520-0493(1983)111<0046:SFSAID>2.0.CO;2

Loshchilov, I., Hutter, F., 2019. Decoupled weight decay regularization. Int. Conf. Learn. Represent. (ICLR 2019).

Mamalakis, A., Barnes, E.A., Ebert-Uphoff, I., 2022. Investigating the fidelity of explainable artificial intelligence methods for applications of convolutional neural networks in geoscience. Artif. Intell. Earth Syst. 1, e220012. https://doi.org/10.1175/AIES-D-22-0012.1

Mann, H.B., 1945. Nonparametric tests against trend. Econometrica 13, 245-259. https://doi.org/10.2307/1907187

Mazumder, T., Saroar, M.M., 2025. Lightning-induced vulnerability assessment in Bangladesh using machine learning and GIS-based approach. Prog. Disaster Sci. 25, 100406. https://doi.org/10.1016/j.pdisas.2025.100406

McGovern, A., Lagerquist, R., Gagne, D.J., Jergensen, G.E., Elmore, K.L., Homeyer, C.R., Smith, T., 2019. Making the black box more transparent: understanding the physical implications of machine learning. Bull. Am. Meteorol. Soc. 100, 2175-2199. https://doi.org/10.1175/BAMS-D-18-0195.1

Micikevicius, P., Narang, S., Alben, J., Diamos, G., Elsen, E., Garcia, D., Ginsburg, B., Houston, M., Kuchaiev, O., Venkatesh, G., Wu, H., 2018. Mixed precision training. Int. Conf. Learn. Represent. (ICLR 2018).

Miglani, V., Yang, A., Markosyan, A., Garcia-Olano, D., Kokhlikyan, N., 2023. Using Captum to explain generative language models, in: Proceedings of the 3rd Workshop for Natural Language Processing Open Source Software (NLP-OSS 2023). Association for Computational Linguistics, Singapore, pp. 165-173. https://doi.org/10.18653/v1/2023.nlposs-1.19

Mongabay, 2026. As lightning strike fatalities increase, Bangladesh still has no reliable preventive measures. Mongabay News, June 2026. https://news.mongabay.com/2026/06/bangladeshs-lightning-death-toll-persists-as-years-of-govt-safeguards-fail/ (accessed 28 September 2026).

Moran, P.A.P., 1950. Notes on continuous stochastic phenomena. Biometrika 37, 17-23. https://doi.org/10.2307/2332142

Mostajabi, A., Finney, D.L., Rubinstein, M., Rachidi, F., 2019. Nowcasting lightning occurrence from commonly available meteorological parameters using machine learning techniques. npj Clim. Atmos. Sci. 2, 41. https://doi.org/10.1038/s41612-019-0098-0

O'Brien, R.M., 2007. A caution regarding rules of thumb for variance inflation factors. Qual. Quant. 41, 673-690. https://doi.org/10.1007/s11135-006-9018-6

Paszke, A., Gross, S., Massa, F., Lerer, A., Bradbury, J., Chanan, G., Killeen, T., Lin, Z., Gimelshein, N., Antiga, L., Desmaison, A., Köpf, A., Yang, E., DeVito, Z., Raison, M., Tejani, A., Chilamkurthy, S., Steiner, B., Fang, L., Bai, J., Chintala, S., 2019. PyTorch: an imperative style, high-performance deep learning library. Adv. Neural Inf. Process. Syst. 32, 8024-8035.

Pesaresi, M., Politis, P., 2023. GHS-BUILT-S R2023A: GHS built-up surface grid, derived from Sentinel-2 composite and Landsat, multitemporal (1975-2030). European Commission, Joint Research Centre. https://doi.org/10.2905/9F06F36F-4B11-47EC-ABB0-4F8B7B1D72EA

Pettitt, A.N., 1979. A non-parametric approach to the change-point problem. J. R. Stat. Soc. C (Appl. Stat.) 28, 126-135. https://doi.org/10.2307/2346729

Ploton, P., Mortier, F., Réjou-Méchain, M., Barbier, N., Picard, N., Rossi, V., Dormann, C.F., Cornu, G., Viennois, G., Bayol, N., Lyapustin, A., Gourlet-Fleury, S., Pélissier, R., 2020. Spatial validation reveals poor predictive performance of large-scale ecological mapping models. Nat. Commun. 11, 4540. https://doi.org/10.1038/s41467-020-18321-y

Price, C., Rind, D., 1992. A simple lightning parameterization for calculating global lightning distributions. J. Geophys. Res. 97(D9), 9919-9933. https://doi.org/10.1029/92JD00719

Rafiuddin, M., Akter, N., Dewan, A., Adnan, M.S.G., Holle, R.L., 2025. Pre-monsoon lightning in Bangladesh: separating most from least active days with thermodynamic and synoptic composites. Atmos. Res. 325, 108261. https://doi.org/10.1016/j.atmosres.2025.108261

Randles, C.A., da Silva, A.M., Buchard, V., Colarco, P.R., Darmenov, A., Govindaraju, R., Smirnov, A., Holben, B., Ferrare, R., Hair, J., Shinozuka, Y., Flynn, C.J., 2017. The MERRA-2 aerosol reanalysis, 1980 onward. Part I: system description and data assimilation evaluation. J. Clim. 30, 6823-6850. https://doi.org/10.1175/JCLI-D-16-0609.1

Reichstein, M., Camps-Valls, G., Stevens, B., Jung, M., Denzler, J., Carvalhais, N., Prabhat, 2019. Deep learning and process understanding for data-driven Earth system science. Nature 566, 195-204. https://doi.org/10.1038/s41586-019-0912-1

Roberts, D.R., Bahn, V., Ciuti, S., Boyce, M.S., Elith, J., Guillera-Arroita, G., Hauenstein, S., Lahoz-Monfort, J.J., Schröder, B., Thuiller, W., Warton, D.I., Wintle, B.A., Hartig, F., Dormann, C.F., 2017. Cross-validation strategies for data with temporal, spatial, hierarchical, or phylogenetic structure. Ecography 40, 913-929. https://doi.org/10.1111/ecog.02881

Rodger, C.J., Werner, S., Brundell, J.B., Lay, E.H., Thomson, N.R., Holzworth, R.H., Dowden, R.L., 2006. Detection efficiency of the VLF World-Wide Lightning Location Network (WWLLN): initial case study. Ann. Geophys. 24, 3197-3214. https://doi.org/10.5194/angeo-24-3197-2006

Romps, D.M., Seeley, J.T., Vollaro, D., Molinari, J., 2014. Projected increase in lightning strikes in the United States due to global warming. Science 346, 851-854. https://doi.org/10.1126/science.1259100

Ronneberger, O., Fischer, P., Brox, T., 2015. U-Net: convolutional networks for biomedical image segmentation, in: Medical Image Computing and Computer-Assisted Intervention (MICCAI 2015), LNCS 9351. Springer, Cham, pp. 234-241. https://doi.org/10.1007/978-3-319-24574-4_28

Rosenfeld, D., Lohmann, U., Raga, G.B., O'Dowd, C.D., Kulmala, M., Fuzzi, S., Reissell, A., Andreae, M.O., 2008. Flood or drought: how do aerosols affect precipitation? Science 321, 1309-1313. https://doi.org/10.1126/science.1160606

Schiavina, M., Freire, S., Carioli, A., MacManus, K., 2023. GHS-POP R2023A: GHS population grid multitemporal (1975-2030). European Commission, Joint Research Centre. https://doi.org/10.2905/2FF68A52-5B5B-4A22-8F40-C41DA8332CFE

Schlemper, J., Oktay, O., Schaap, M., Heinrich, M., Kainz, B., Glocker, B., Rueckert, D., 2019. Attention gated networks: learning to leverage salient regions in medical images. Med. Image Anal. 53, 197-207. https://doi.org/10.1016/j.media.2019.01.012

Sen, P.K., 1968. Estimates of the regression coefficient based on Kendall's tau. J. Am. Stat. Assoc. 63, 1379-1389. https://doi.org/10.1080/01621459.1968.10480934

Shi, X., Chen, Z., Wang, H., Yeung, D.-Y., Wong, W.-K., Woo, W.-C., 2015. Convolutional LSTM network: a machine learning approach for precipitation nowcasting. Adv. Neural Inf. Process. Syst. 28, 802-810.

Sundararajan, M., Taly, A., Yan, Q., 2017. Axiomatic attribution for deep networks. Proc. 34th Int. Conf. Mach. Learn. (ICML), PMLR 70, 3319-3328.

Thornton, J.A., Virts, K.S., Holzworth, R.H., Mitchell, T.P., 2017. Lightning enhancement over major oceanic shipping lanes. Geophys. Res. Lett. 44, 9102-9111. https://doi.org/10.1002/2017GL074982

UNDRR, 2017. Report of the open-ended intergovernmental expert working group on indicators and terminology relating to disaster risk reduction (A/71/644). United Nations Office for Disaster Risk Reduction, Geneva.

Virts, K.S., Wallace, J.M., Hutchins, M.L., Holzworth, R.H., 2013. Highlights of a new ground-based, hourly global lightning climatology. Bull. Am. Meteorol. Soc. 94, 1381-1391. https://doi.org/10.1175/BAMS-D-12-00082.1

Wan, Z., Hook, S., Hulley, G., 2015. MOD11A2 MODIS/Terra Land Surface Temperature/Emissivity 8-Day L3 Global 1km SIN Grid V006. NASA EOSDIS Land Processes DAAC. https://doi.org/10.5067/MODIS/MOD11A2.006

Wang, Z., Bovik, A.C., Sheikh, H.R., Simoncelli, E.P., 2004. Image quality assessment: from error visibility to structural similarity. IEEE Trans. Image Process. 13, 600-612. https://doi.org/10.1109/TIP.2003.819861

Weiss, D.J., Nelson, A., Gibson, H.S., Temperley, W., Peedell, S., Lieber, A., Hancher, M., Poyart, E., Belchior, S., Fullman, N., Mappin, B., Dalrymple, U., Rozier, J., Lucas, T.C.D., Howes, R.E., Tusting, L.S., Kang, S.Y., Cameron, E., Bisanzio, D., Battle, K.E., Bhatt, S., Gething, P.W., 2018. A global map of travel time to cities to assess inequalities in accessibility in 2015. Nature 553, 333-336. https://doi.org/10.1038/nature25181

Wilcoxon, F., 1945. Individual comparisons by ranking methods. Biometrics Bull. 1, 80-83. https://doi.org/10.2307/3001968

Wilks, D.S., 2016. “The stippling shows statistically significant grid points”: how research results are routinely overstated and overinterpreted, and what to do about it. Bull. Am. Meteorol. Soc. 97, 2263-2273. https://doi.org/10.1175/BAMS-D-15-00267.1

Williams, E.R., 2005. Lightning and climate: a review. Atmos. Res. 76, 272-287. https://doi.org/10.1016/j.atmosres.2004.11.014

Yamane, Y., Hayashi, T., Dewan, A.M., Akter, F., 2010a. Severe local convective storms in Bangladesh: Part I. Climatology. Atmos. Res. 95, 400-406. https://doi.org/10.1016/j.atmosres.2009.11.004

Yamane, Y., Hayashi, T., Dewan, A.M., Akter, F., 2010b. Severe local convective storms in Bangladesh: Part II. Environmental conditions. Atmos. Res. 95, 407-418. https://doi.org/10.1016/j.atmosres.2009.11.003

Yuan, T., Remer, L.A., Pickering, K.E., Yu, H., 2011. Observational evidence of aerosol enhancement of lightning activity and convective invigoration. Geophys. Res. Lett. 38, L04701. https://doi.org/10.1029/2010GL046052

Zhou, K., Zheng, Y., Dong, W., Wang, T., 2020. A deep learning network for cloud-to-ground lightning nowcasting with multisource data. J. Atmos. Ocean. Technol. 37, 927-942. https://doi.org/10.1175/JTECH-D-19-0146.1

Appendix A. Supplementary tables

Table A1. Model input channels after collinearity screening (order as in the data cube). Mean and SD are 2012-2020 training statistics over the modelling mask (in log1p space where transformed).

#	Channel	Description	Source	log1p	Mean	SD
0	CAPE	convective available potential energy	ERA5	√	5.060	1.929
1	CIN	convective inhibition (0 where undefined)	ERA5	√	3.057	2.406
2	TT	Total Totals index	ERA5 (derived)	-	37.49	6.679
3	CP	convective precipitation	ERA5	√	1.210	0.842
4	BLH	boundary-layer height (m)	ERA5	-	391.1	143.8
5	D2M	2 m dew point (°C)	ERA5	-	17.97	7.925
6	U10	10 m zonal wind (m s^{-1})	ERA5	-	−0.108	0.814
7	V10	10 m meridional wind (m s^{-1})	ERA5	-	0.288	1.051
8	WS	10 m wind speed	ERA5 (derived)	√	0.665	0.361
9	AOD	aerosol optical depth, 550 nm	MERRA-2	-	0.391	0.193
10	CHIRPS	monthly rainfall (mm)	CHIRPS v2.0	√	4.048	1.847
11	LST_day	daytime land-surface temperature (°C)	MODIS MOD11A2	-	25.81	6.795
12	NDVI	normalised difference vegetation index	MODIS MOD13A3	-	0.603	0.185
13	ELEV_SD	sub-grid elevation SD (m)	SRTM v4.1	√	3.253	1.927
14	DIST_WATER	distance to water (km)	derived from Copernicus LC	√	3.319	0.939
15	CROP_FRAC	cropland fraction	Copernicus LC100	-	0.320	0.284
16	TREE_FRAC	tree-cover fraction	Copernicus LC100	-	0.419	0.318

#	Channel	Description	Source	log1p	Mean	SD
17	WATER_FRAC	water fraction	Copernicus LC100	√	0.057	0.120
18	MASK	binary modelling mask	GADM + land cover	-	-	-

Removed by VIF screening (VIF at removal): T2M 93.3, K-index 36.1, LST night 29.3, slope 18.2, TCWV 13.0, elevation 10.2.

Table A2. Per-run test results (2023-2025, inside Bangladesh) of the final v5 configuration.

Model	Seed	Best epoch	RMSE (log1p)	R^2	CSI
U-Net	42 / 43 / 44	28 / 15 / 14	0.626 / 0.614 / 0.623	0.355 / 0.379 / 0.361	0.304 / 0.265 / 0.248
Attention U-Net	42 / 43 / 44	6 / 8 / 14	0.605 / 0.604 / 0.614	0.398 / 0.400 / 0.379	0.318 / 0.295 / 0.283
ConvLSTM	42 / 43 / 44	2 / 5 / 6	0.602 / 0.605 / 0.612	0.403 / 0.398 / 0.383	0.264 / 0.298 / 0.291
ConvLSTM-U-Net	42 / 43 / 44	11 / 27 / 4	0.603 / 0.629 / 0.615	0.402 / 0.350 / 0.378	0.269 / 0.248 / 0.298
v1 baseline (best, hybrid)	42	-	0.605	0.398	-

Table A3. Spatial four-fold block cross-validation, test 2023-2025, held-out block ∩ Bangladesh (RMSE / R^2 / CSI, log1p).

Fold	U-Net	Attn U-Net	ConvLSTM	Hybrid	CV ensemble	Climatology	CAPE × P
NW (418 cells)	.602/.122/.35	.613/.092/.32	.570/.214/.34	.623/.062/.35	.589/.162/.35	.558/.247/.27	.517/.352/.30
NE (458)	.677/.363/.11	.660/.395/.10	.670/.377/.08	.639/.432/.20	.652/.410/.11	.713/.293/.13	.690/.338/.00
SW (445)	.611/.265/.28	.609/.269/.27	.617/.249/.30	.608/.272/.27	.599/.295/.28	.639/.196/.06	.601/.289/.16
SE (452)	.727/.266/.26	.710/.298/.16	.678/.360/.18	.732/.255/.09	.696/.327/.14	.732/.254/.09	.668/.380/.10
Mosaic (all BD)	.657/.289/.26	.650/.304/.23	.637/.333/.27	.653/.298/.24	.636/.334/.26	.666/.269/.15	.625/.357/.08

Climatology uses the local observed history of the held-out block (information advantage). The proxy is refitted per fold without the held-out block.

Table A4. Regional means relative to the Bangladesh mean, and rank (1 = highest), for the satellite and model products.

Region	TRMM/ISS-LIS	WGLC 2012-2025	Ensemble test	CV mosaic rank
Sylhet	1.52 (#1)	1.71 (#1)	1.67 (#1)	#1
Rangpur	1.24 (#2)	0.99 (#5)	0.94 (#6)	#2
Mymensingh	1.22 (#3)	1.14 (#2)	1.11 (#2)	#5
Dhaka	1.14 (#4)	0.98 (#6)	0.95 (#5)	#6
Chittagong	0.92 (#5)	1.10 (#4)	1.00 (#4)	#8
CHT hills	0.91 (#6)	1.13 (#3)	1.00 (#3)	#9
Rajshahi	0.84 (#7)	0.70 (#9)	0.80 (#9)	#3
Khulna	0.72 (#8)	0.77 (#7)	0.85 (#8)	#7
Barisal	0.60 (#9)	0.72 (#8)	0.92 (#7)	#4
Rank agreement with satellite (Spearman)	-	0.75	0.70	0.43 (proxy 0.13)

Table A5. Pairwise tests on monthly test scores: mean difference (A − B), moving-block bootstrap 95 % CI and Holm-adjusted Wilcoxon p (* p < 0.05). RMSE: 36 months; CSI: 24 months with a defined hotspot set.

Pair (A − B)	ΔRMSE	95 % CI	p (Holm)	ΔCSI	p (Holm)
U-Net − Attn U-Net	+0.011	[+0.006, +0.018]	0.029 *	+0.001	1.000
U-Net − ConvLSTM	+0.012	[+0.004, +0.022]	1.000	+0.008	1.000
U-Net − Hybrid	+0.002	[−0.007, +0.010]	1.000	+0.012	1.000
U-Net − Ensemble	+0.021	[+0.015, +0.028]	< 0.001 *	+0.013	0.867
U-Net − Climatology	−0.040	[−0.074, −0.007]	0.029 *	+0.026	1.000
U-Net − Persistence	−0.185	[−0.263, −0.121]	< 0.001 *	−0.066	0.168
U-Net − CAPE×P	+0.001	[−0.021, +0.026]	1.000	+0.067	0.013 *
Attn U-Net − ConvLSTM	+0.000	[−0.006, +0.007]	1.000	+0.007	1.000
Attn U-Net − Hybrid	−0.010	[−0.019, −0.001]	1.000	+0.011	1.000
Attn U-Net − Ensemble	+0.009	[+0.007, +0.013]	< 0.001 *	+0.012	0.447
Attn U-Net − Climatology	−0.051	[−0.087, −0.021]	0.009 *	+0.025	0.912
Attn U-Net − Persistence	−0.196	[−0.278, −0.138]	< 0.001 *	−0.067	0.122
Attn U-Net − CAPE×P	−0.010	[−0.032, +0.011]	1.000	+0.066	0.020 *
ConvLSTM − Hybrid	−0.010	[−0.021, +0.000]	1.000	+0.003	1.000

Pair (A − B)	ΔRMSE	95 % CI	p (Holm)	ΔCSI	p (Holm)
ConvLSTM − Ensemble	+0.009	[+0.003, +0.016]	0.368	+0.004	1.000
ConvLSTM − Climatology	−0.051	[−0.085, −0.022]	0.011 *	+0.017	1.000
ConvLSTM − Persistence	−0.197	[−0.275, −0.135]	< 0.001 *	−0.075	0.027 *
ConvLSTM − CAPE×P	−0.010	[−0.033, +0.013]	1.000	+0.058	0.002 *
Hybrid − Ensemble	+0.019	[+0.012, +0.028]	< 0.001 *	+0.001	1.000
Hybrid − Climatology	−0.041	[−0.075, −0.010]	0.011 *	+0.014	1.000
Hybrid − Persistence	−0.187	[−0.266, −0.124]	< 0.001 *	−0.078	0.059
Hybrid − CAPE×P	−0.000	[−0.024, +0.025]	1.000	+0.055	0.022 *
Ensemble − Climatology	−0.060	[−0.098, −0.029]	0.002 *	+0.013	1.000
Ensemble − Persistence	−0.206	[−0.288, −0.143]	< 0.001 *	−0.079	0.059
Ensemble − CAPE×P	−0.019	[−0.043, +0.004]	1.000	+0.054	0.060
Climatology − Persistence	−0.145	[−0.216, −0.085]	< 0.001 *	−0.092	0.010 *
Climatology − CAPE×P	+0.041	[+0.015, +0.069]	0.016 *	+0.041	0.094
Persistence − CAPE×P	+0.186	[+0.117, +0.275]	< 0.001 *	+0.133	< 0.001 *

Negative ΔRMSE and positive ΔCSI favor system A.

Table A6. Seasonal upazila risk (quintiles within each season; ensemble hazard 2016-2025).

Season	Spearman ρ vs annual	Top-50 overlap	Top-3 upazilas
MAM	0.859	46	Jaintiapur, Gowainghat, Kanaighat (Sylhet; Meghalaya foothills)
JJAS	0.877	29	Tahirpur, Dakshin Sunamganj, Derai (Sunamganj haor)
September	0.769	23	Tahirpur, Dakshin Sunamganj, Langadu (Rangamati, CHT)

Table A7. The 50 highest-risk upazilas (primary annual risk). Hazard in strokes km^{-2} yr^{-1} (ensemble, 2016-2025).

Rank	Upazila	District	Pop. 2025 (thousand)	Hazard (annual)	Hazard (MAM)	Risk	P(high or very high)	Class, satellite H	Dominant driver
1	Tahirpur	Sunamganj	220	2.38	3.92	0.563	1.00	VH	CHIRPS
2	Dakshin Sunamganj	Sunamganj	250	2.29	3.95	0.555	1.00	VH	CHIRPS
3	Jaintiapur	Sylhet	222	2.29	5.28	0.549	0.98	VH	CHIRPS
4	Gowainghat	Sylhet	283	2.34	5.22	0.545	0.99	VH	CHIRPS
5	Bishwambarpur	Sunamganj	212	2.42	4.16	0.526	1.00	VH	CHIRPS
6	Jamalganj	Sunamganj	163	2.23	3.44	0.517	0.99	VH	CHIRPS
7	Kanaighat	Sylhet	355	2.17	5.07	0.506	0.97	VH	CHIRPS
8	Dowarabazar	Sunamganj	283	2.51	4.91	0.504	1.00	VH	CHIRPS
9	Chhatak	Sunamganj	468	2.28	4.63	0.498	0.99	VH	CHIRPS
10	Sunamganj Sadar	Sunamganj	368	2.44	4.31	0.494	1.00	VH	CHIRPS
11	Companiganj	Sylhet	237	2.44	5.25	0.493	0.99	VH	CHIRPS
12	Derai	Sunamganj	290	2.08	3.39	0.490	0.99	VH	CHIRPS
13	Dharampasha	Sunamganj	239	2.07	3.34	0.451	0.99	VH	CHIRPS
14	Bishwanath	Sylhet	264	2.14	4.76	0.434	0.98	VH	CHIRPS
15	Sulla	Sunamganj	150	1.86	2.90	0.419	0.98	VH	CHIRPS
16	Jagannathpur	Sunamganj	334	2.00	3.99	0.418	0.99	H	CHIRPS
17	Khaliajuri	Netrakona	116	1.84	2.80	0.392	0.98	VH	CHIRPS
18	Zakiganj	Sylhet	367	1.97	4.61	0.391	0.95	VH	CHIRPS
19	Kalmakanda	Netrakona	349	1.90	3.37	0.391	0.99	VH	CHIRPS
20	Golabganj	Sylhet	411	2.03	4.80	0.390	0.97	H	CHIRPS
21	Mohanganj	Netrakona	199	1.85	3.01	0.374	0.98	VH	CHIRPS
22	Beani Bazar	Sylhet	349	1.97	4.73	0.371	0.95	VH	CHIRPS
23	Fenchuganj	Sylhet	143	1.83	4.23	0.359	0.97	H	CHIRPS

Rank	Upazila	District	Pop. 2025 (thousand)	Hazard (annual)	Hazard (MAM)	Risk	P(high or very high)	Class, satellite H	Dominant driver
24	Balaganj	Sylhet	410	1.91	4.32	0.356	0.98	VH	CHIRPS
25	Barlekha	Maulvibazar	396	1.78	4.17	0.346	0.96	VH	CHIRPS
26	Sylhet Sadar	Sylhet	759	2.26	5.10	0.342	0.98	VH	CHIRPS
27	Dakshin Surma	Sylhet	748	2.11	4.87	0.337	0.97	M	CHIRPS
28	Rajnagar	Maulvibazar	326	1.76	4.01	0.336	0.97	VH	CAPE
29	Itna	Kishoreganj	210	1.67	2.59	0.326	0.96	VH	CHIRPS
30	Mithamain	Kishoreganj	113	1.59	2.45	0.321	0.93	VH	CHIRPS
31	Ajmiriganj	Habiganj	145	1.67	2.78	0.321	0.97	VH	CHIRPS
32	Durgapur	Netrakona	267	1.73	3.18	0.302	0.97	VH	CAPE
33	Nabiganj	Habiganj	405	1.70	3.58	0.295	0.97	H	CHIRPS
34	Baniachong	Habiganj	435	1.60	3.00	0.292	0.95	VH	CHIRPS
35	Juri	Maulvibazar	150	1.69	3.78	0.291	0.93	VH	CAPE
36	Barhatta	Netrakona	240	1.69	3.04	0.291	0.95	VH	CHIRPS
37	Dhobaura	Mymensingh	229	1.62	3.04	0.282	0.95	VH	CAPE
38	Maulvi Bazar Sadar	Maulvibazar	413	1.70	3.80	0.277	0.95	H	CAPE
39	Madan	Netrakona	195	1.61	2.73	0.277	0.95	VH	CHIRPS
40	Atpara	Netrakona	186	1.57	2.91	0.272	0.95	VH	CAPE
41	Kulaura	Maulvibazar	480	1.65	3.68	0.272	0.93	VH	CAPE
42	Austagram	Kishoreganj	197	1.46	2.40	0.259	0.89	VH	CAPE
43	Langadu	Rangamati	71	1.48	1.39	0.255	0.89	VH	CAPE
44	Sreemangal	Maulvibazar	415	1.58	3.35	0.247	0.93	H	CAPE
45	Bhurungamari	Kurigram	253	1.53	2.18	0.243	0.92	VH	CAPE
46	Kamalganj	Maulvibazar	379	1.58	3.33	0.242	0.92	VH	CAPE
47	Lakhai	Habiganj	195	1.43	2.54	0.233	0.88	VH	CAPE

Rank	Upazila	District	Pop. 2025 (thousand)	Hazard (annual)	Hazard (MAM)	Risk	P(high or very high)	Class, satellite H	Dominant driver
48	Bahubal	Habiganj	279	1.57	3.36	0.233	0.91	H	CAPE
49	Tarail	Kishoreganj	198	1.49	2.67	0.227	0.92	H	CAPE
50	Haluaghat	Mymensingh	376	1.46	2.78	0.226	0.91	H	CAPE

All 50 are in the very-high class with no uncertain class (modal-class probability 0.78-1.00). None of the 50 is an urban thana or city corporation unit. Satellite-hazard classes: VH very high, H high, M moderate. Dominant driver: dynamic predictor with the largest mean |IG| (Section 3.5). Austagram, Langadu and Lakhai have P(high or very high) < 0.9, so they are not among the 50 upazilas with P ≥ 0.9 reported in the text; the other 47 are in both sets. The full ranking of all 545 units (GADM level-3; see Section 2.1) is available from the corresponding author on reasonable request.

Appendix B. Supplementary figures

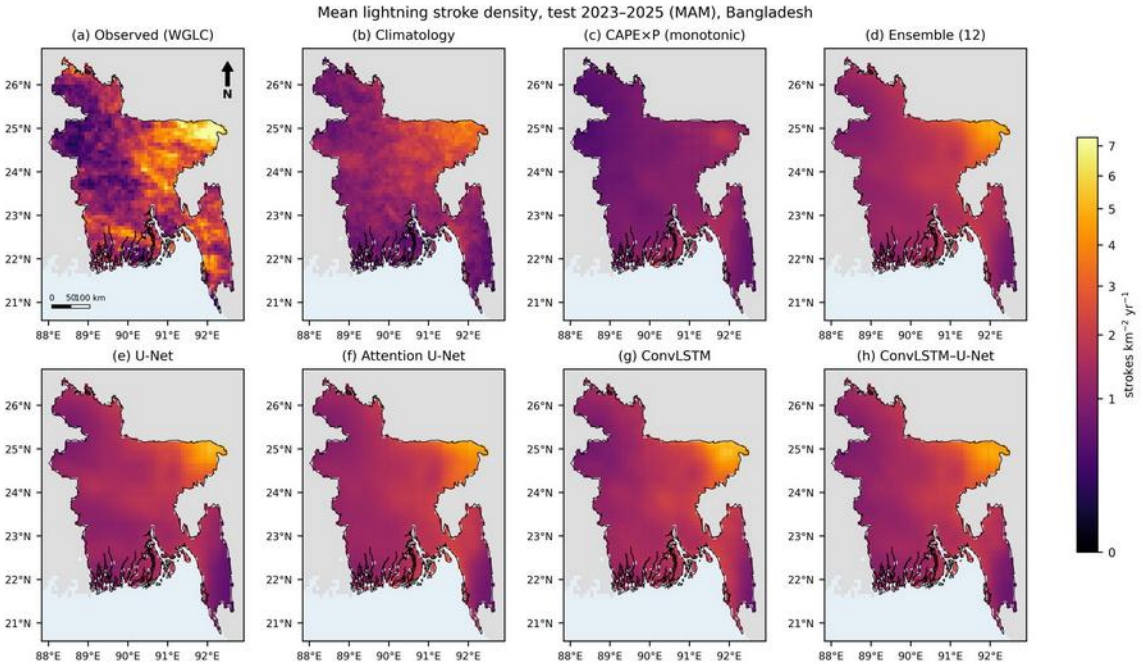


Figure B1. Pre-monsoon (MAM) mean stroke density, test 2023-2025: (a) observed, (b) climatology, (c) CAPE × P proxy, (d) ensemble, (e-h) the four architectures. Shared square-root color scale.

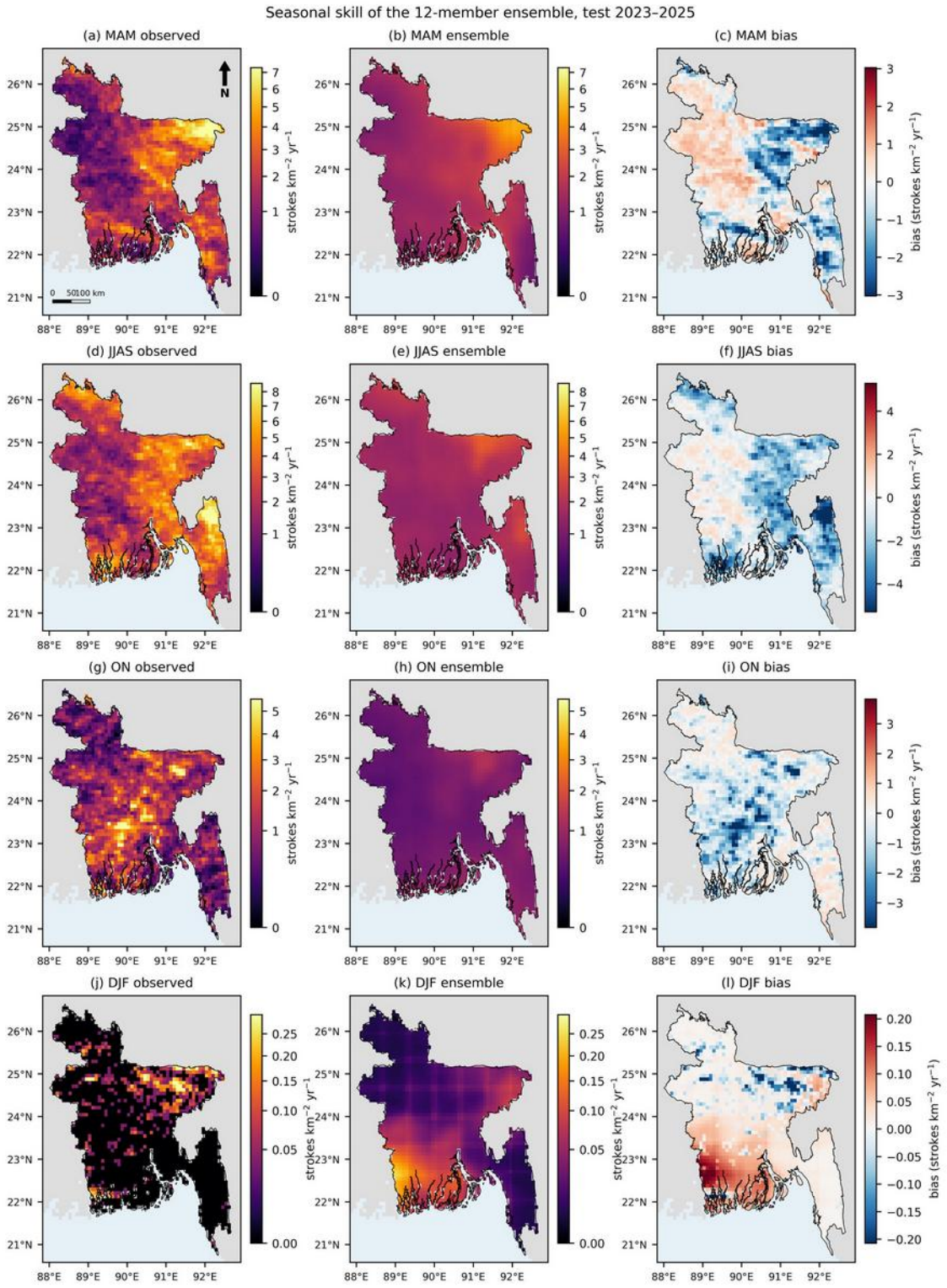


Figure B2. Seasonal performance of the ensemble, test 2023-2025: observed, ensemble and bias maps for MAM, JJAS, ON and DJF.

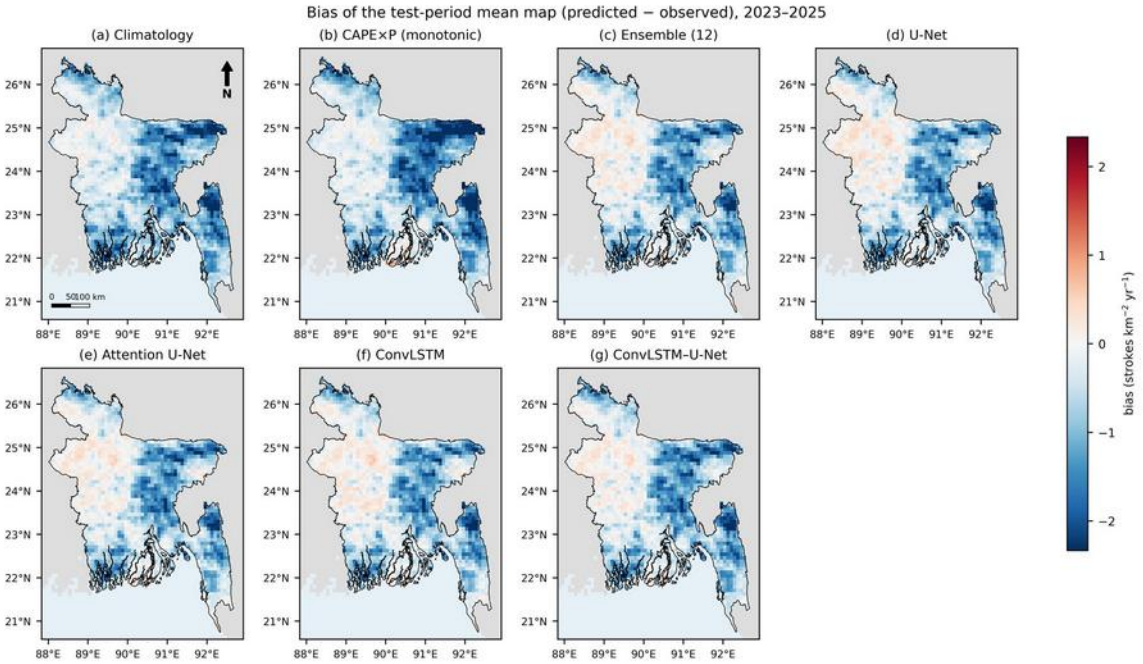


Figure B3. Bias of the test-period mean map (predicted − observed) for climatology, the proxy, the ensemble and the four architectures.

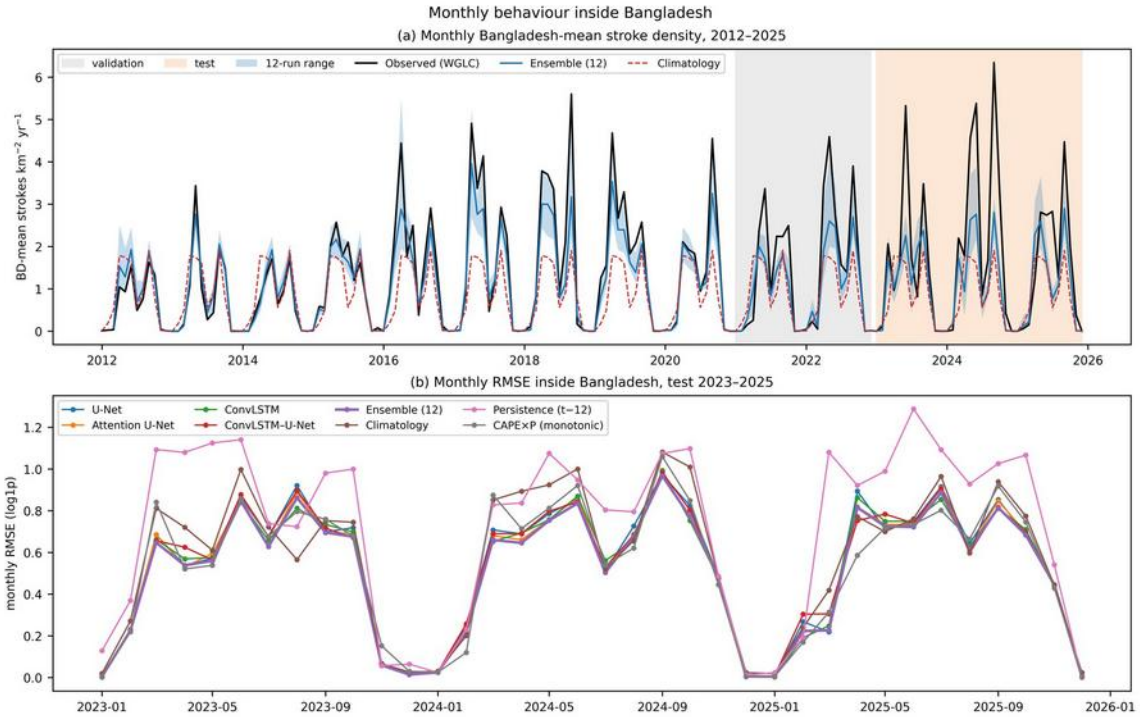


Figure B4. (a) Monthly Bangladesh-mean stroke density 2012-2025, observed and predicted (training, validation and test periods shaded); (b) monthly RMSE of all systems in the test period.

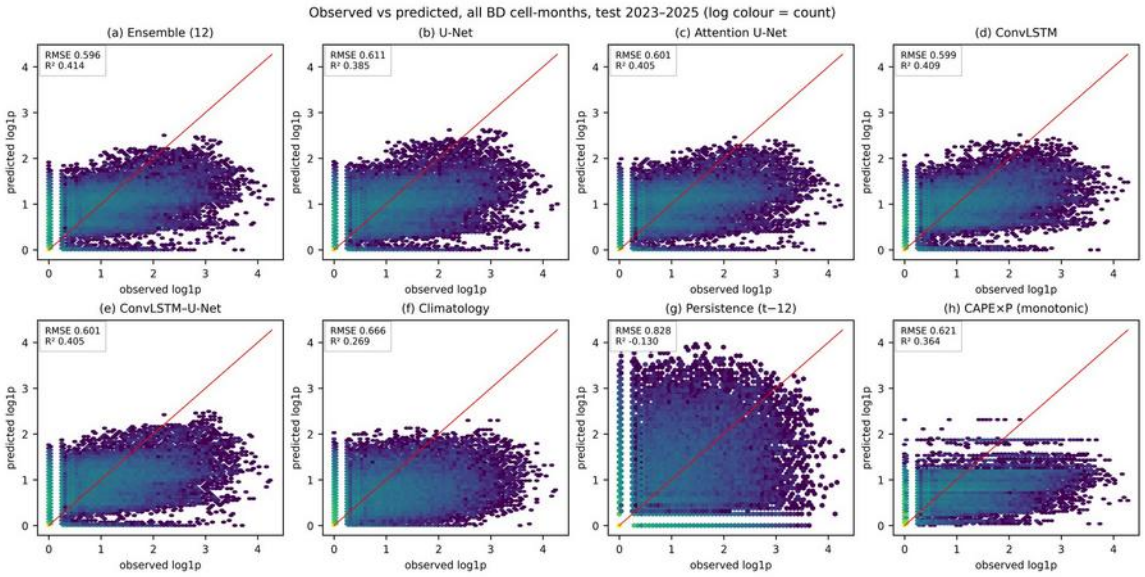


Figure B5. Observed against predicted log density for all Bangladesh cell-months of the test period (color = count, log scale) for the ensemble, the four architectures and the three baselines.

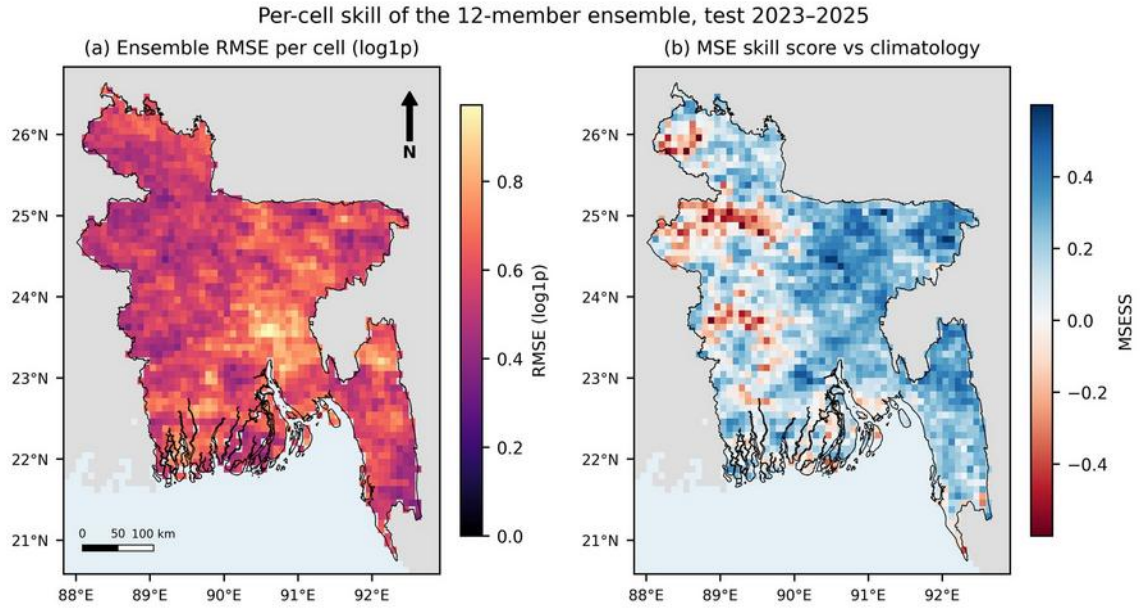


Figure B6. Per-cell skill of the ensemble, test 2023-2025: (a) RMSE (log1p) and (b) MSE skill score relative to climatology.

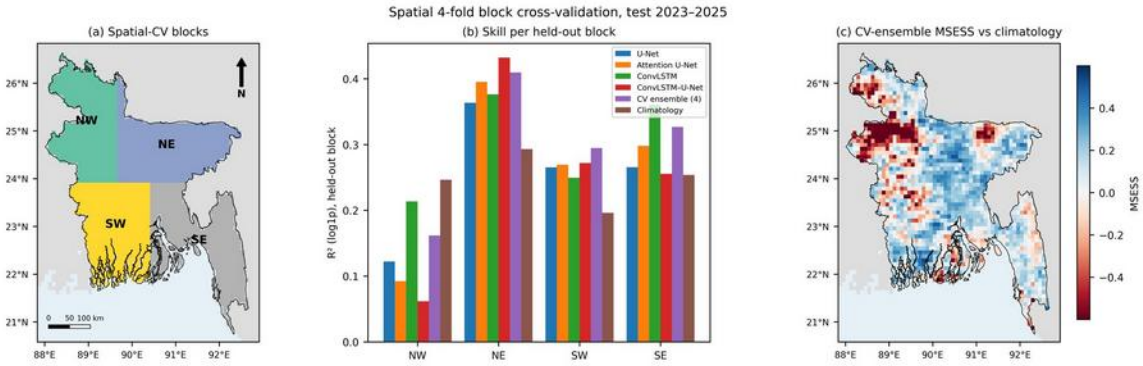


Figure B7. Spatial four-fold block cross-validation: (a) blocks, (b) R^2 per held-out block for each architecture, the CV ensemble and climatology, (c) CV-ensemble MSESS relative to climatology.

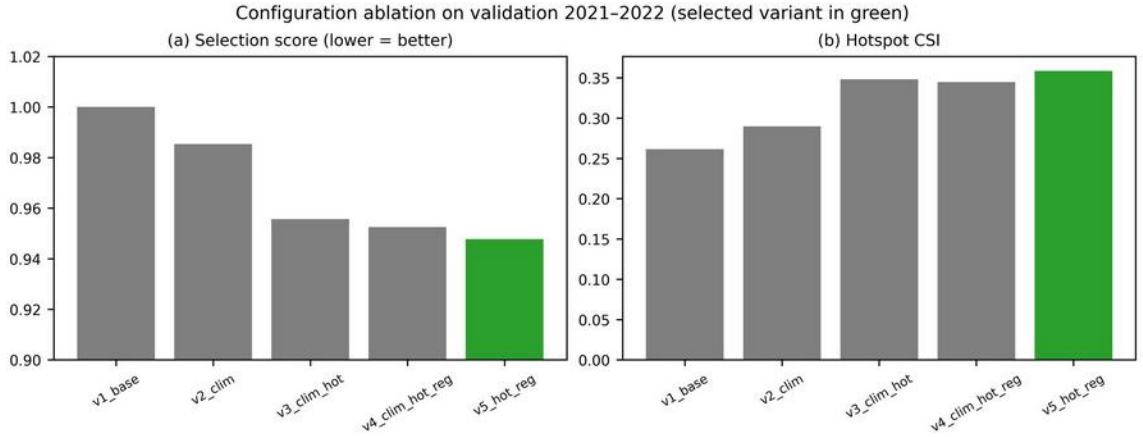


Figure B8. Validation-only configuration ablation (2021-2022): (a) predefined selection score (lower is better; selected variant highlighted) and (b) hotspot CSI by variant and architecture.

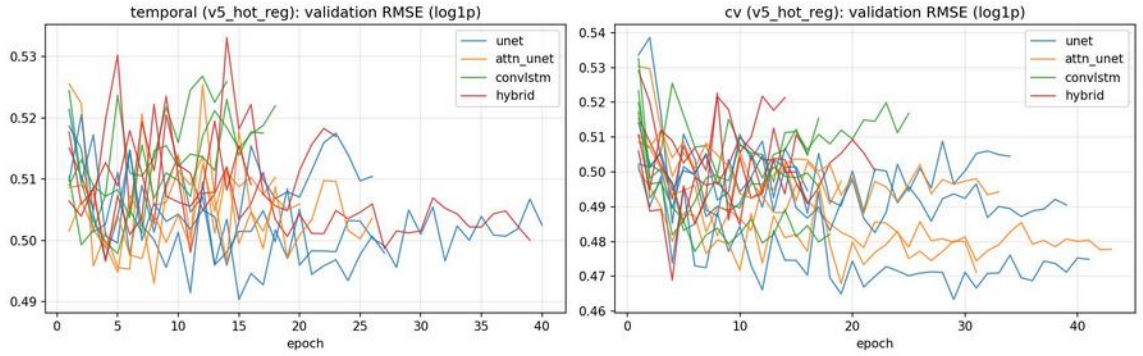


Figure B9. Training and validation curves of the final runs (Phase 4 training log).

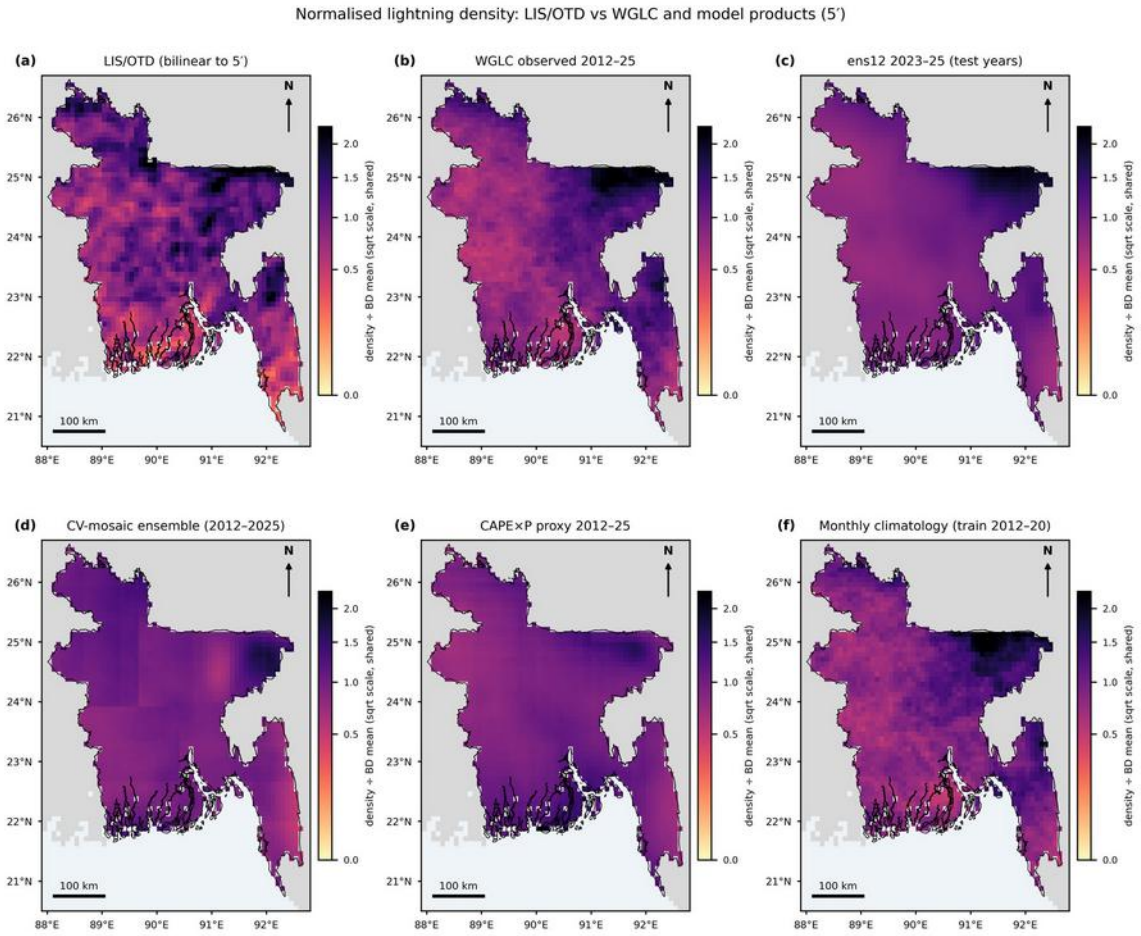


Figure B10. Normalized 5′ maps (each ÷ its Bangladesh mean, shared square-root scale): (a) satellite climatology, (b) WGLC 2012-2025, (c) ensemble on test years, (d) CV-mosaic ensemble, (e) CAPE × P proxy, (f) climatology. Panel labels “LIS/OTD” denote the combined TRMM-LIS/ISS-LIS climatology.

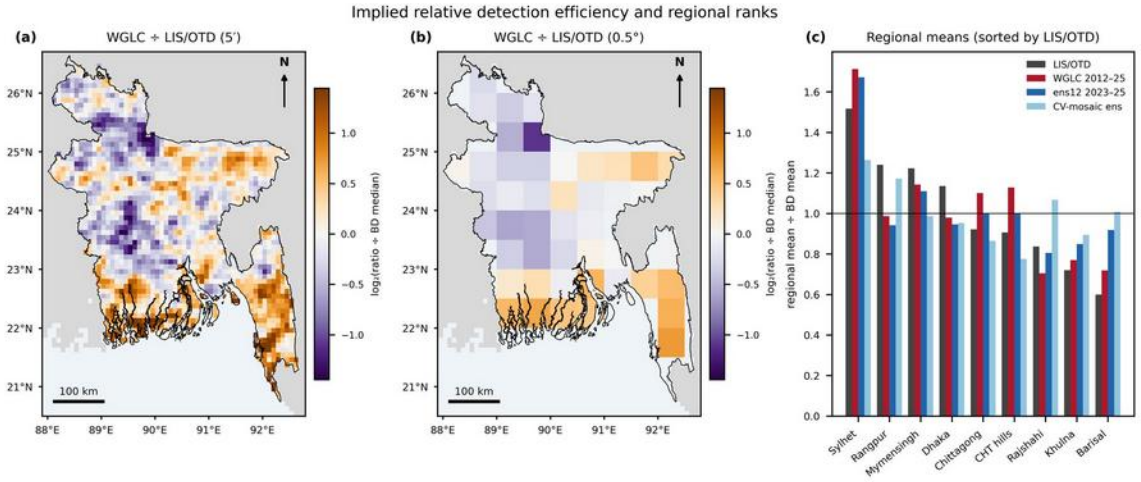


Figure B11. Implied relative detection efficiency: $\log_2$ of the WGLC ÷ satellite ratio relative to its Bangladesh median at (a) 5′ and (b) 0.5°, and (c) regional means relative to the Bangladesh mean for the satellite, WGLC, ensemble (test) and CV mosaic.

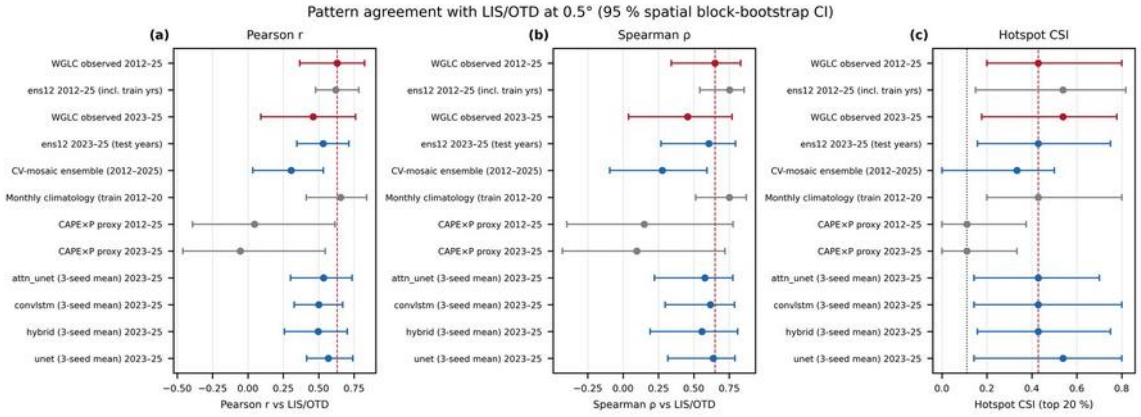


Figure B12. Summary of pattern agreement with the satellite climatology at 0.5°: (a) Pearson r, (b) Spearman ρ and (c) hotspot CSI with 95 % spatial block-bootstrap intervals.

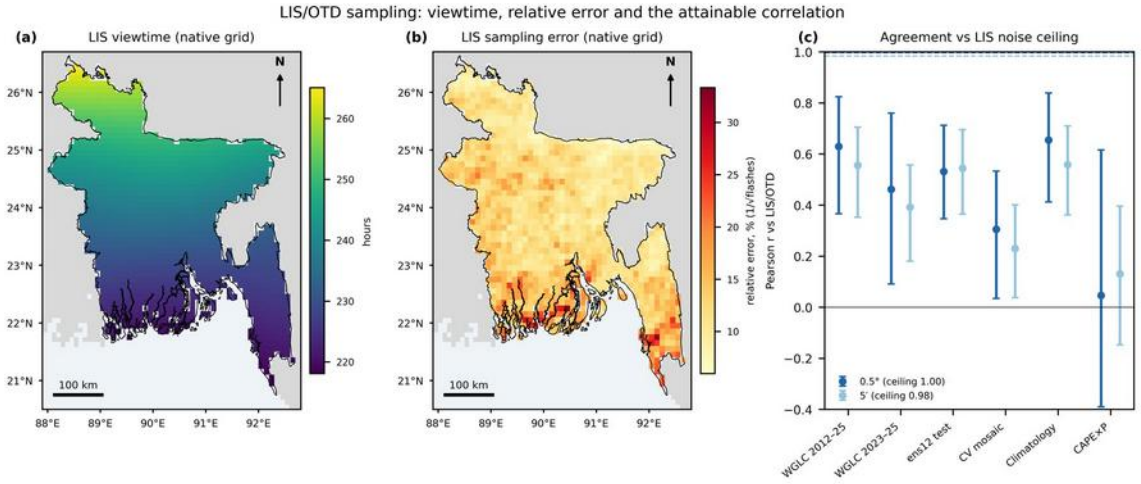


Figure B13. Satellite sampling: (a) view time, (b) Poisson relative sampling error and (c) observed correlations against the noise ceiling.

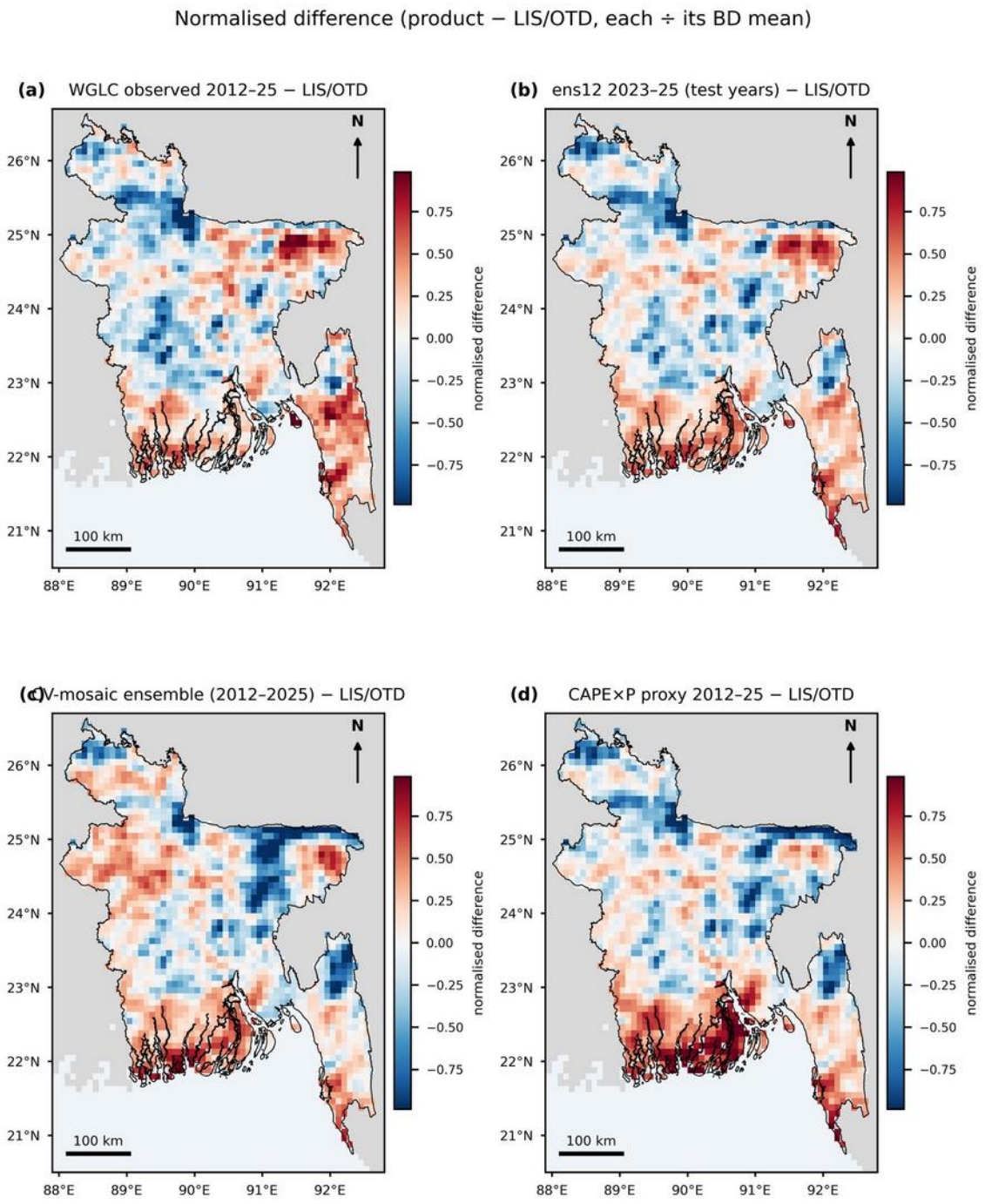


Figure B14. Normalized differences (product − satellite, each ÷ its Bangladesh mean) for WGLC, the ensemble on test years, the CV mosaic and the proxy.

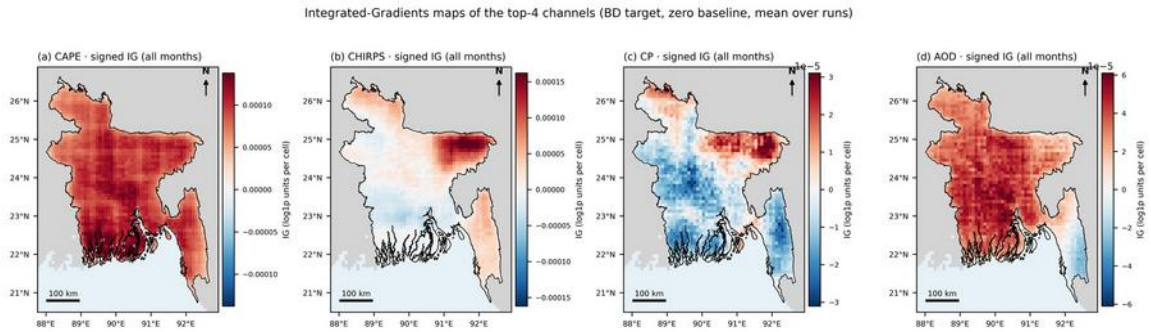


Figure B15. Signed Integrated-Gradients maps (all test months, mean over runs) of (a) CAPE, (b) CHIRPS, (c) convective precipitation and (d) AOD.

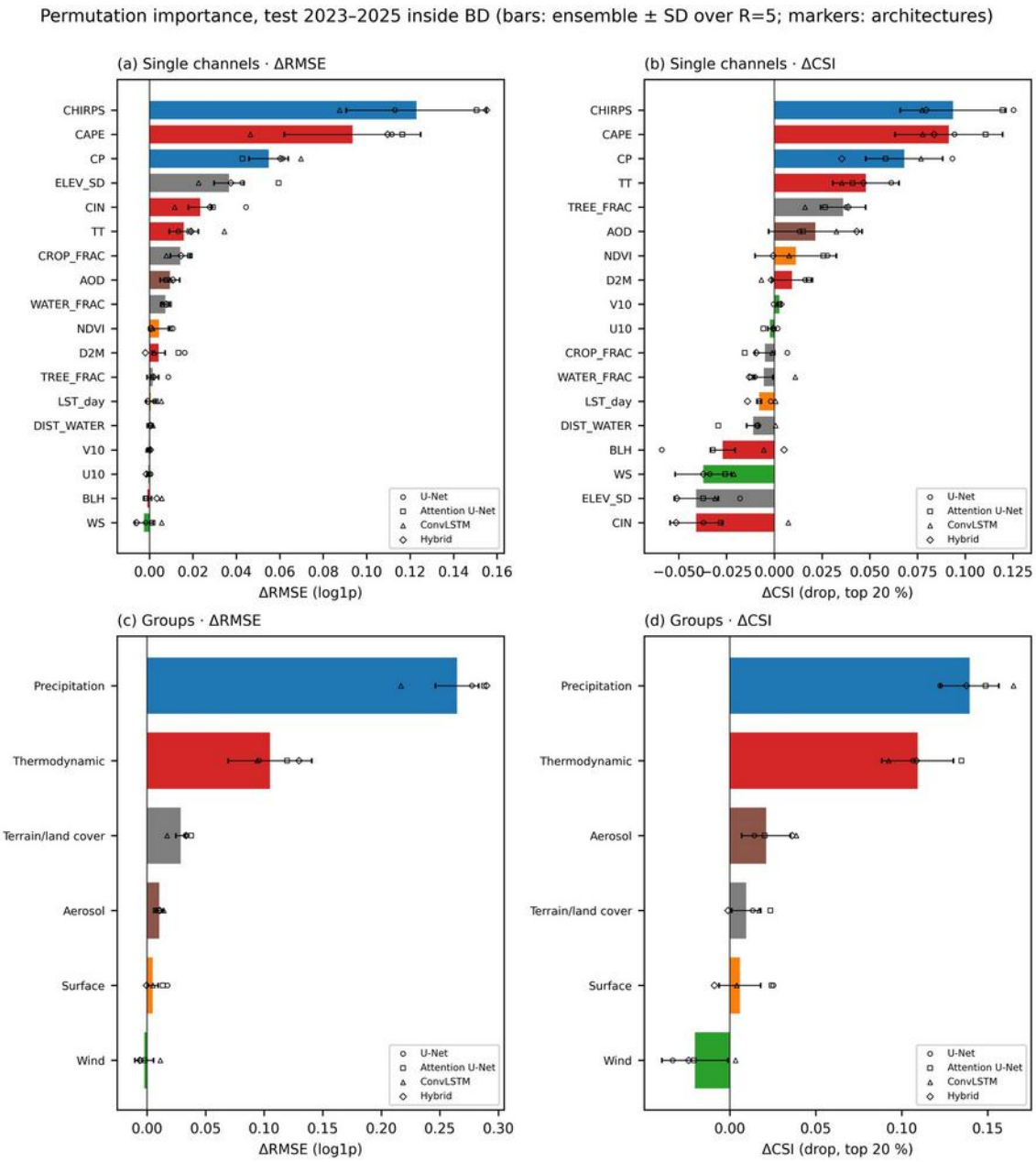


Figure B16. Permutation importance on the test years: single channels (a) ΔRMSE and (b) ΔCSI; groups (c) ΔRMSE and (d) ΔCSI. Bars: ensemble ± SD over repeats; markers: architectures.

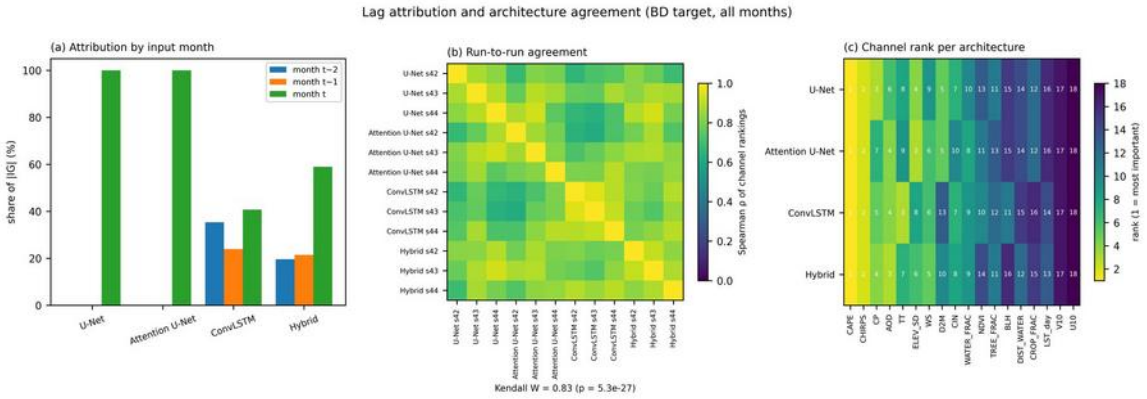


Figure B17. (a) Share of IG attribution by input month for each architecture; (b) Spearman correlation of channel rankings between the 12 runs (Kendall's W = 0.83); (c) channel rank per architecture.

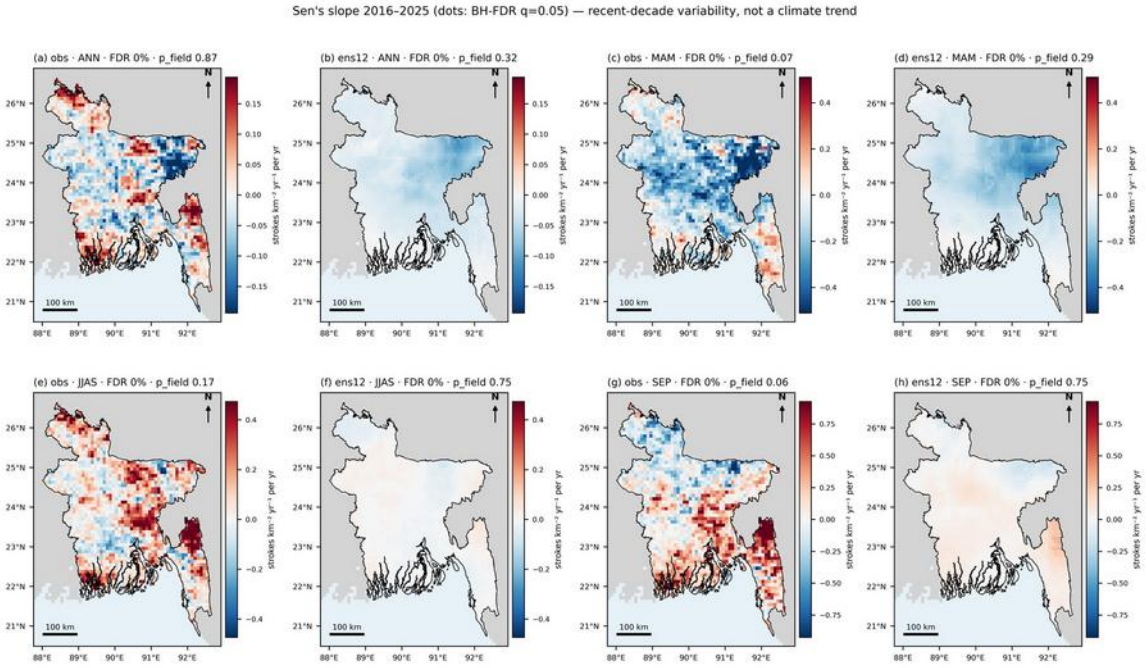


Figure B18. Sen's slope 2016-2025 of observed WGLC and ensemble density (annual, MAM, JJAS, September); dots would mark BH-FDR-significant cells (none). Recent-decade variability, not a climate trend.

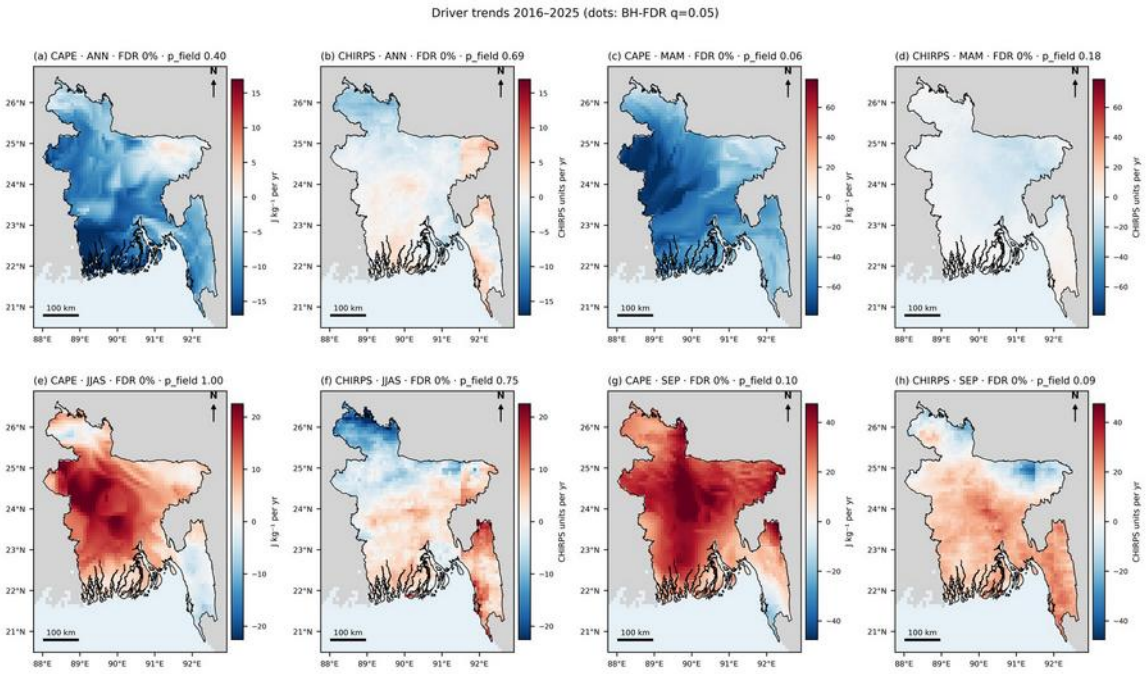


Figure B19. Sen's slope 2016-2025 of CAPE and CHIRPS (annual, MAM, JJAS, September). The straight north-south discontinuity near 91.5°E in CHIRPS is a product artefact.

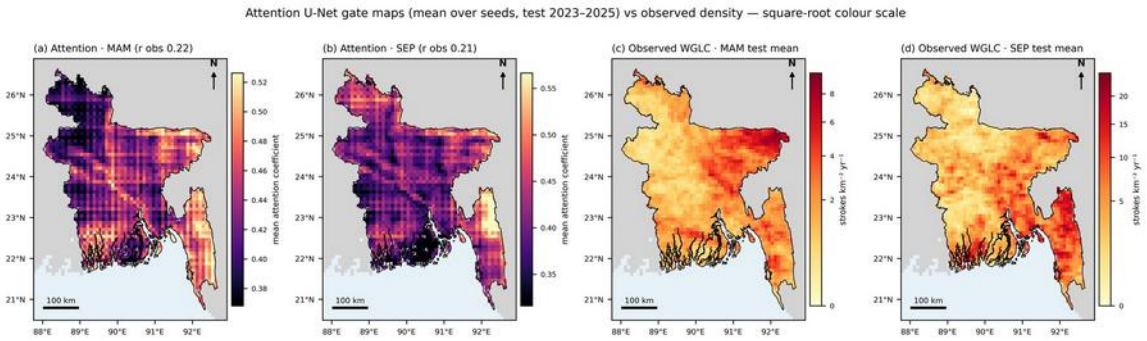


Figure B20. Attention-gate maps of the Attention U-Net (mean over seeds) for MAM and September with the observed density. Attention was inconsistent across seeds (r = 0.03-0.41) and shows a patch-grid artefact; it is not interpreted physically.

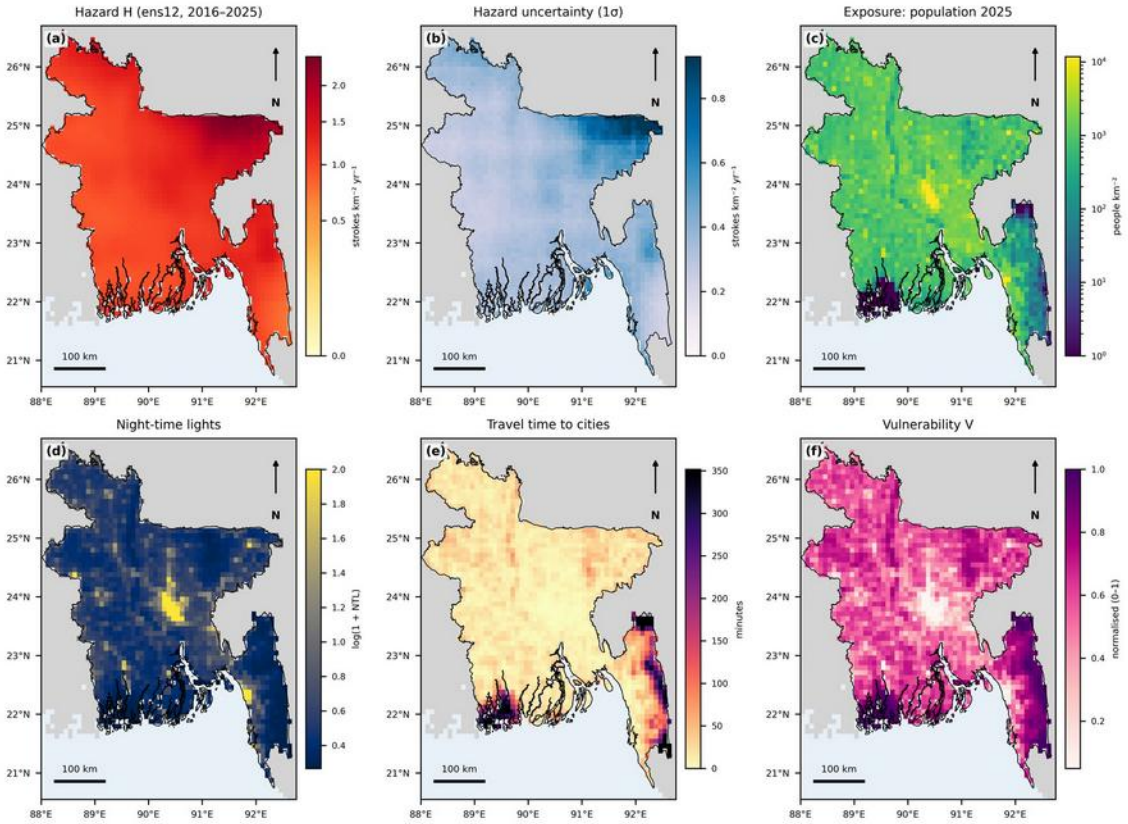


Figure B21. Risk components, 2016-2025: (a) hazard (ensemble density), (b) hazard uncertainty (1σ of Monte-Carlo draws), (c) population density, (d) night-time lights, (e) travel time to cities, (f) vulnerability index.

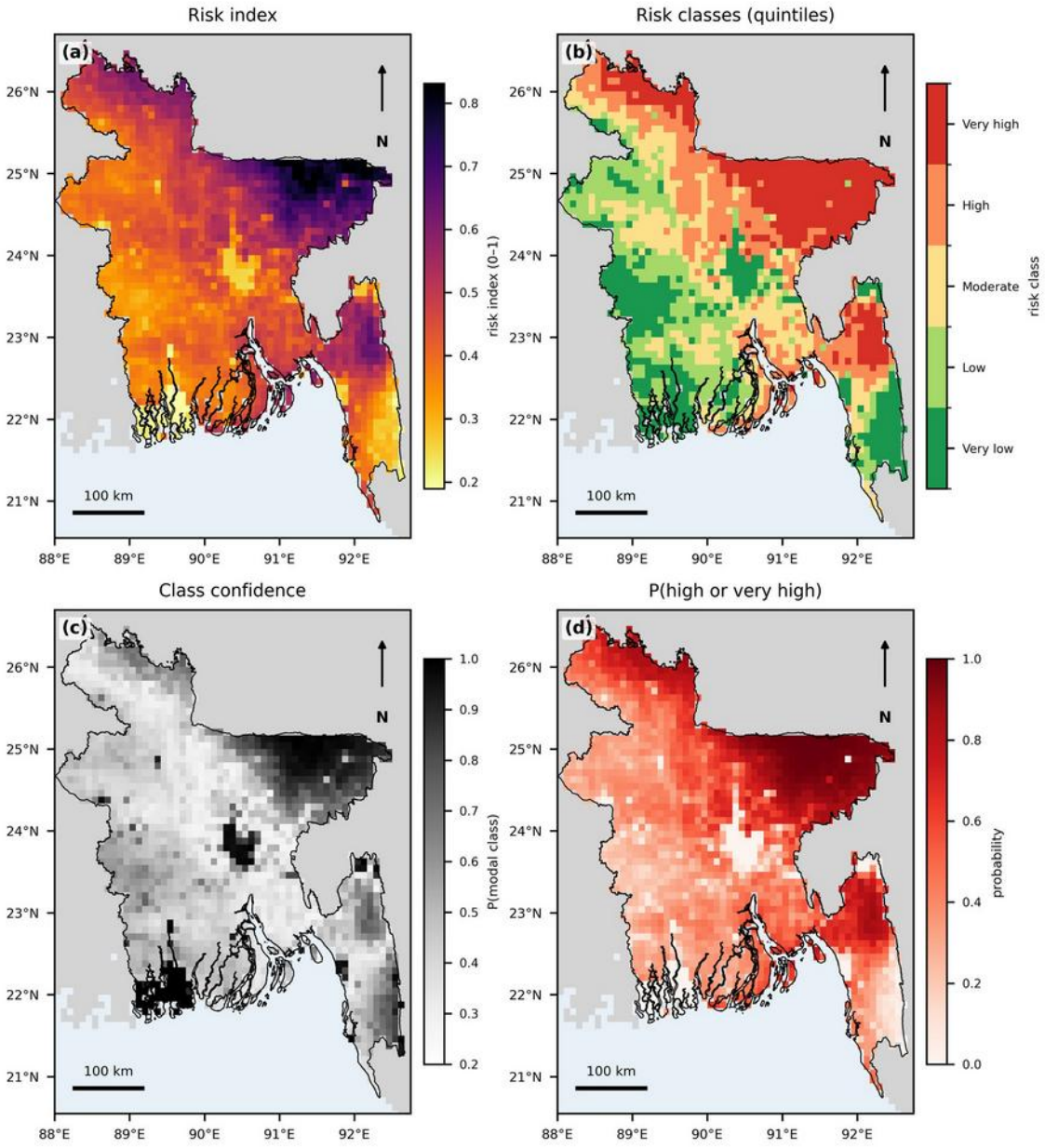


Figure B22. Pixel-level risk: (a) risk index $(H \cdot E \cdot V)^{1/3}$, (b) quintile classes, (c) Monte-Carlo confidence (probability of the modal class) and (d) P(high or very high).

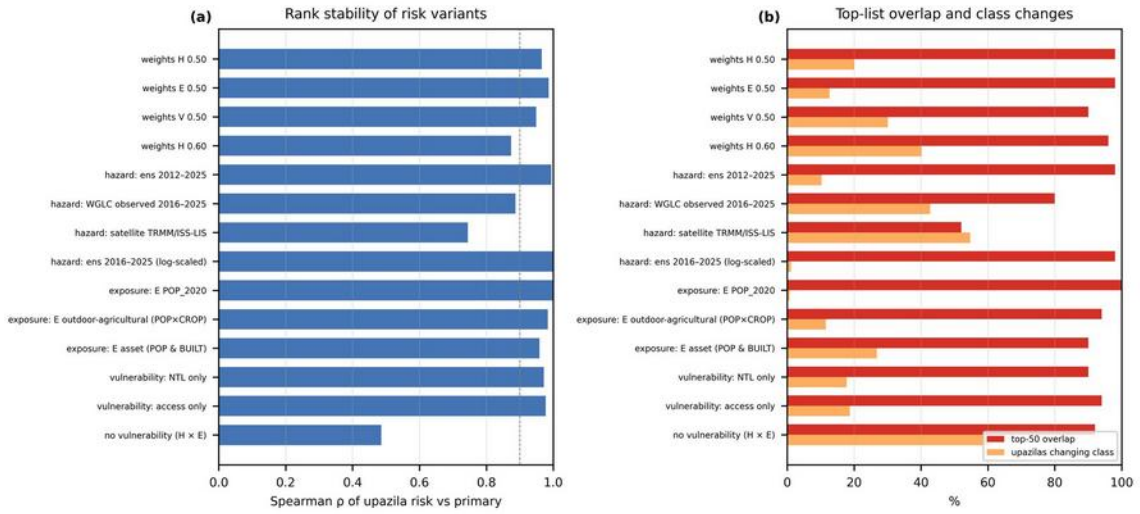


Figure B23. Sensitivity of the upazila ranking: (a) Spearman ρ with the primary ranking and (b) top-50 overlap for each variant.

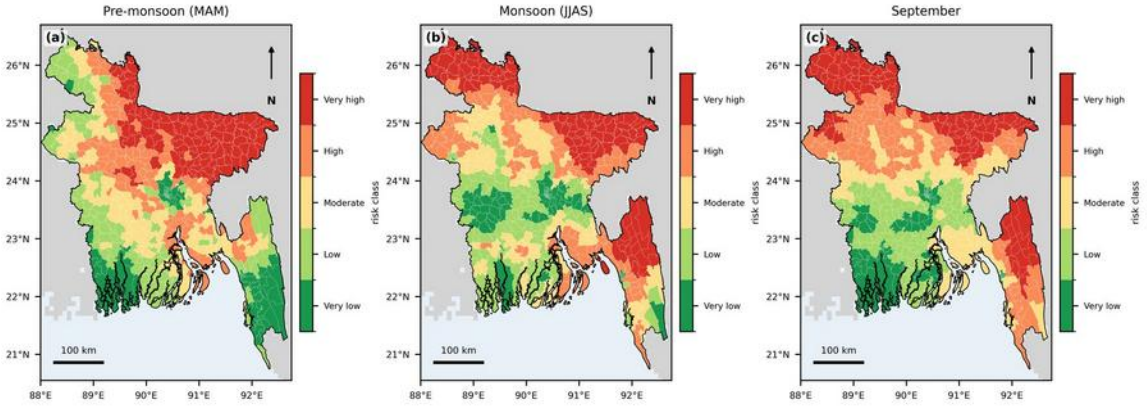


Figure B24. Seasonal upazila risk classes (quintiles within each season): (a) MAM, (b) JJAS and (c) September.

Appendix C. Supplementary methods

C.1 Pre-processing details

ERA5 (0.25°) and MERRA-2 AOD (0.5° × 0.625°) were interpolated bilinearly to the 5′ grid. Because this is up sampling, conservative remapping was not required. After re gridding, domain means differed from the source by less than 1.7 %. Every time axis was normalized to month-start dates before merging. CIN is undefined where there is no convection (41.6 % of values), and we set it to zero, meaning no inhibition, before re gridding. MODIS LST was screened for residual cloud contamination with a per-pixel, per-calendar-month robust *z*-score (median and median absolute deviation from 2012-2020; $|z| > 4$ flagged; 0.82 % of daytime and 0.44 % of night-time values). Gaps were filled in three steps: linear temporal interpolation over at most two months, then the 2012-2020 same-month climatology, then the nearest neighbor. Monsoon gaps reached 8.0 % for daytime LST and 13.7 % for night-time LST. CHIRPS and NDVI had no gaps over land.

C.2 Permutation importance

Permutation importance (Breiman, 2001) provided a model-agnostic cross-check. It is the increase in test RMSE, and the loss of hotspot CSI, when a predictor is permuted (five repeats). Dynamic predictors were permuted by shuffling whole monthly maps across the 38 months feeding the test windows. Static predictors were permuted by shuffling 1° tiles among land tiles. Correlated predictors were also permuted jointly within six physical groups: precipitation, thermodynamic, wind, aerosol, surface, and terrain/land cover. Attention-gate maps of the Attention U-Net were inspected but are reported only in the Appendix because they were unstable across seeds.

C.3 Error correlation for risk uncertainty

A moment estimator of ρ from standardized residuals proved unstable: 0.06 on validation but 0.91 on test, because σ_{cal} approaches zero in dry months. ρ was therefore set by coverage calibration, as the smallest value giving 90 % coverage of the observed 2021-2022 mean map ($\rho = 0.07$). It was then checked on the 2023-2025 mean map. One thousand log-normal hazard realizations $H^{(b)}$ were drawn. Draws were independent between cells for pixel-level class probabilities, and spatially coherent for upazila-level class and rank probabilities, using a Gaussian random field with an e-folding length of 50 km. An upazila's class was flagged *uncertain* if its modal-class probability was below 0.6. We report P(high or very high) as a decision layer.

C.4 Implementation and reproducibility

Data were acquired with Google Earth Engine, the Copernicus Climate Data Store and NASA GES DISC/GHRC. Pre-processing ran in Google Colab. Model training (v2 full commit, 1.8 h), evaluation, validation, explainability (91.9 min on a T4 GPU) and risk analysis (172 s on CPU) ran as single-cell Kaggle notebooks. Each notebook completed a reduced “smoke” run before the committed full run and printed explicit pass/fail checks at every step. All random seeds are recorded.